The Ideal Strength of Materials: Elastic, Magnetic, and Phonon Instabilities

by

David Michael Clatterbuck

B.S. (Iowa State University) 1998
M.S. (Iowa State University) 1998

A dissertation submitted in partial satisfaction of the
requirements for the degree of
Doctor of Philosophy

in

Engineering - Materials Science and Engineering

in the

GRADUATE DIVISION
of the
UNIVERSITY OF CALIFORNIA, BERKELEY

Committee in charge:
Professor J. W. Morris Jr., Chair
Associate Professor Daryl C. Chrzan
University Professor Marvin L. Cohen

Spring 2003

The Ideal Strength of Materials: Elastic, Magnetic, and Phonon Instabilities

Copyright 2003
by
David Michael Clatterbuck

Abstract

The Ideal Strength of Materials:
Elastic, Magnetic, and Phonon Instabilities

by

David Michael Clatterbuck
Doctor of Philosophy in Engineering - Materials Science and Engineering

University of California, Berkeley

Professor J. W. Morris Jr., Chair

Electronic structure calculations based on density functional theory have been used to study the role of elastic, magnetic, and phonon instabilities in determining the ideal strength of iron and aluminum.

In <001> tension the ideal strength of iron is determined by an elastic instability in the ferromagnetic phase along the "Bain" path from bcc to fcc. Instabilities with respect to transformation into a face centered orthorhombic structure and into various magnetic structures occur but are encountered at larger strains and, thus, do not affect the ideal strength. The ideal shear strengths of iron in two prominent shear systems, <111>{112} and <111>{110}, are very similar due to the fact that both loading configurations lead to the same body centered tetragonal saddle point structure. Magnetic instabilities also occur during <111>{112} shear but do not affect the strength because they appear at larger the strains than the elastic instabiliy. The ideal tensile strength in the [001] direction is increased when one applies a biaxial tensile stress in the (001) plane while biaxial compression has the opposite effect. A simple crystallographic model is able to explain this result. While Fe exhibits some novel effects due to magnetism, they do not affect the ideal strength which is determined by the same elastic instabilities found in most other bcc metals.

In aluminium the saddle point structures and, hence, the failure modes are identical for quasi-static <110> tension and <112>{111} shear; however, the maximum resolved shear stresses are quite different. This effect is explained by examining the elastic energy associated with different components of the stress and strain tensors. For quasi-static loading in <100> and <111> uniaxial tension the only saddle point structures occur at infinite strain

which would lead physically to cleavage fracture. However, in <111> tension an orthogonal elastic instability occurs before the peak in the stress-strain curve and produces a shear failure. For all four of the loading configurations considered, computations of the phonon dispersion as a function of strain reveal phonon instabilities that occur at points away from the center of the Brillouin zone before the material becomes elastically unstable. This is the first time the ideal strength of a simple metal has been shown to be dictated by phonon instabilities. All of the unstable modes have a shear character suggesting that shear failure is an inherent property of aluminum even in an initially dislocation-free perfect crystal.

Contents

List of Figures iii

List of Tables vii

1 The Ideal Strength 1
- 1.1 Relevance of the ideal strength . . . 2
- 1.2 Phase transformations and the ideal strength . . . 4

2 Iron: Elastic and Magnetic Instabilities 9
- 2.1 Introduction . . . 9
- 2.2 Computational methods . . . 12
- 2.3 Equilibrium structures . . . 14
- 2.4 Ideal strength in tension . . . 19
  - 2.4.1 Tetragonal versus orthorhombic instability . . . 19
  - 2.4.2 Magnetic instabilities . . . 23
  - 2.4.3 Comparison with previous calculations and experiment . . . 24
- 2.5 Ideal strength in shear . . . 25
  - 2.5.1 Shear strength of FM bcc Fe . . . 25
  - 2.5.2 Magnetic instabilities . . . 29
- 2.6 Ideal strength in multiaxial loading . . . 31
- 2.7 Conclusions . . . 34

3 Aluminum: elastic and phonon instabilities 37
- 3.1 Introduction . . . 37
- 3.2 Computational methods . . . 38
- 3.3 The quasi-static ideal strength of Al . . . 39
  - 3.3.1 <110> tension and <112>{111} shear . . . 39
  - 3.3.2 <100> tension and <111> tension . . . 50
- 3.4 Phonon instabilities in aluminum and its ideal strength . . . 53
- 3.5 Conclusions . . . 59

4 Summary and future work 63
- 4.1 Summary . . . 63
- 4.2 Future Work . . . 64

4.2.1 Temperature dependence of the ideal strength 64
4.2.2 Analysis of nanoindentation data 66

Bibliography **69**

List of Figures

2.1 The bcc crystal structure becomes the fcc structure after fully relaxed elongation along the <100> direction. 11

2.2 The energy as a function of strain has an extremum at the fcc structure which can be a local maximum (solid line) or minimum (dotted line). Assuming sinusoidal form, the inflection point governing the ideal strength falls at a much lower strain in the latter case, and the ideal strength is significantly less. 11

2.3 The energy and magnetic moment per atom as functions of volume computed using the PAW method for Fe in the bcc (filled symbols) and fcc (open symbols) crystal structures for several magnetic states: (diamonds) non-magnetic (NM), (squares) ferromagnetic (FM), (circles) antiferromagnetic (AFM), and (triangles) double period antiferromagnetic (DAFM). The discontinuity in the fcc FM curve separates two distinct phases with different magnetic moments. 16

2.4 The energy and magnetic moment per atom as functions of volume computing using the FLAPW method for Fe in the bcc (filled symbols) and fcc (open symbols) crystal structures for several magnetic states: (diamonds) non-magnetic (NM), (squares) ferromagnetic (FM), (circles) antiferromagnetic (AFM), and (triangles) double period antiferromagnetic (DAFM). The discontinuity in the fcc FM curve separates two distinct phases with different magnetic moments. The energy-volume relation for the ground state spiral spin density wave of fcc Fe [47] is indicated by the points labeled (+). These are plotted relative to the minimum in the AFM curve to correct for a small, consistent difference in the energies calculated by Knöpfle et al. [47]. 17

2.5 (a) Energy and (b) stress as a function of applied tensile strain along <001>: (filled squares) Bain Path with tetragonal symmetry, (open square) orthorhombic path. (c) Ratios of the lattice parameters along the orthorhombic path: (filled diamond) a/b, (filled triangle) a/c, (filled circle) b/c. Numbers and open circles an (a) and (c) indicate special structures with high symmetry that are shown schematically in Figure 2.6. 20

2.6 The geometry of the Bain path and the orthorhombic instability. The crystal starts as a bcc structure (1) which can also be visualized as a fco structure with a:b:c ratio of $\sqrt{2} : \sqrt{2} : 1$. If tetragonal symmetry is maintained the Bain path is followed to the fcc structure (4) which is equivalent to a bct structure with a c/a ratio of $\sqrt{2}$. If the tetragonal symmetry is broken the orthorhombic path is followed and a maximum energy is reached at a special bct structure (2) which has a c/a ratio of 1.66. From that energy maxima, the orthorhombic path leads down in energy to a bcc structure (3) which is rotated relative to the starting bcc structure. 21
2.7 Energy versus strain in the <001> direction for various magnetic structures: (solid square) bct-FM, (open square) fco-FM, (filled triangle) bct-DAFM, (open triangle) fco-DAFM, (filled circle) bct-AFM, (filled diamond) bct-LSFM. The fco-AFM and fco-LSFM structures follow paths identical to bct-AFM and bct-LSFM respectively and are not shown. A magnetic phase transformation is seen near 20% strain. Lines are guides for the eye. 24
2.8 (a) Energy versus shear strain and (b) absolute value of the stress versus strain for (filled square) <111>{112} shear and (open square) <111>{110} shear. 26
2.9 Geometry of the <111>{112} shear system. The base centered monoclinic cell is shown inside the initial bcc structure (left). A {110} projection of the structure shows the how the monoclinic cell becomes a bct cell upon applying a ∼33% shear in the easy direction (top). A shear in the opposite (hard) direction generates a base centered orthorhombic structure after a shear strain of ∼66% (bottom). The monoclinic structure's two fold axis is pointed out of the page. Black atoms are those in the closest plane and the gray atoms are in the following plane of atoms. 28
2.10 The magnetic structures used to describe complex magnetic ordering in <111>{112} shear. The structures are supercells made up of 1 or 2 body centered monoclinic cells whose 2-fold axes are oriented out of the page. The bct-DAFM structure is shown for reference. 30
2.11 Energy as a function of shear strain for several magnetic structures. (solid square) FM, (open square) DAFMX, (open circle) DAFMZ, (open triangle) DAFMY, (open diamond) DAFMY2, (X) AFM. The various magnetic structures are shown in Figure 2.10. 30
2.12 Stress as a function of strain for FM Fe under 3 different multiaxial loads: uniaxial tension plus biaxial compression (triangle), uniaxial tension (square), uniaxial tension plus biaxial tension (diamond). In all cases the largest tensile stress is in the [001] direction. The large symbols with arrows indicate the location of tetragonal to orthorhombic instabilities. The loading configuration which includes biaxial compression was not tested for this type of instability. 32

3.1 Phonon dispersion of Al measured experimentally at 80K (open symbols) [72] and calculated using the 0K LDA lattice parameter (filled symbols). 40
3.2 Stress versus strain for (diamonds) <110> uniaxial tension and (triangles) relaxed <112>{111} shear. 41

3.3 Relaxation strains in Al (filled symbols) and Cu (open symbols) due to applied tensile strain in the [110] direction: (triangles) $[\bar{1}10]$ relaxation, (squares) [001] relaxation. The dashed line indicates the points where the nearest neighbor distances in the [110] and [001] directions are equal giving rise to tetragonal symmetry. 42

3.4 Schematics showing the evolution of the crystal structure during $[11\bar{2}](111)$ shear (top) and [110] tension (bottom). The two dimensional figures are views in the $[\bar{1}10]$ direction. The gray atoms are in the closest (110) plane while the while atoms are in the (110) plane behind it. These gray/white atom positions are repeated in successive (110) planes. For both loading configurations the structure changes from fcc to a stress-free bct structure to a rotated fcc structure. 43

3.5 Resolved shear stress as a function of engineering shear strain for Al along the loading paths corresponding to [110] uniaxial tension (filled symbols) and relaxed $[11\bar{2}](111)$ shear (open symbols). Following the curves backward from 71% shear strain corresponds to [001] uniaxial compression (filled symbols) and relaxed $[\bar{1}\bar{1}2](111)$ shear (open symbols). 44

3.6 Relaxation strains as a function of engineering shear strain for Al along the loading paths corresponding to <110> uniaxial tension (filled symbols) and relaxed <112>{111}shear (open symbols). On the left side, which corresponds to [110] tension and $[11\bar{2}](111)$ shear, the largest relaxations are in the same direction for both tension and shear. However, on the right side, which corresponds to [001] compression and $[\bar{1}\bar{1}2](111)$ shear, the relaxations are in different directions. Along the tensile loading path, the relaxations undergo a dramatic changes near 35% strain. At this strain, the corresponding relaxation strains for the tensile and shear paths are equal to each other (as emphasized by the arrows), demonstrating that both paths cross through the same saddle point structure. 47

3.7 Schematics illustrating the direction of the normal and shearing stresses resolved on the (111) plane for different loading configurations. The gray shaded plane in the 3-dimensional picture corresponds to the gray shaded planes in the $[\bar{1}10]$ views. We see that [110] tension is similar to $[11\bar{2}](111)$ shear but also includes a normal stress acting to expand the crystal in the [111] direction. In addition, [001] compression is similar to $[\bar{1}\bar{1}2](111)$ shear but also includes a normal stress acting to compress the crystal in the [111] direction. 48

3.8 Stress versus engineering strain for uniaxial tension in the (squares) <100> direction and (triangles) <111> direction. The large open triangle indicates the location of the orthogonal elastic instability that occurs during <111> tension. 51

3.9 Eigenvalues of the symmetrized Wallace tensor as a function of strain for uniaxial tension in the <111> direction. The lowest eigenvalue is doubly degenerate due to symmetry, and at 25% strain it becomes negative indicating the material is elastically unstable. At 31% strain the second smallest eigenvalue goes to zero corresponding to the tensile modulus in the <111> direction vanishing at the peak in the stress-strain curve. 52
3.10 Stress-strain curves for <110>, <100>, and <111> uniaxial tension as well as relaxed <112>{111} shear. Open circles indicate the location of phonon instabilities. The large triangle indicates the location of the orthogonal elastic instability that occurs in <111> tension. The lines are guides for the eye. . . 53
3.11 Phonon frequencies as a function of strain for (a) [110] tension and (b) $[11\overline{2}](111)$ shear. The curves are labeled according to the applied strain as indicated on the right side of the figure. Lines are spline fits which are guides to the eye. (c) Schematic illustrating the crystallography of the instability at the zone edge. 55
3.12 (a) Phonon frequencies as a function of strain for [001] tension. (b) Schematic of the instabilities. 57
3.13 (a) Electronic density of states as a function of strain in the [001] direction for 0%, 5%, 10%, 15%, and 20% strain. The energies are plotted relative to the Fermi energy which is taken as 0. (b) Band structure for 0% (dashed line), 10% (dot-dashed line), 20% (solid line) strains. Coordinates of symmetry points in units of $2\pi/a$: X=(1 0 0); Z=(0 0 a/c); P=(1 0 a/2c); X'=(1 0 a/c) (Also see Figure 3.14). Arrows emphasize the gap at the X point for 20% strain. 58
3.14 One-eighth of the Fermi surface of Al as a function of strain in the [001] direction. The surface shown corresponds to the second zone and thus the states behind this surface are not occupied by electrons. The Brillouin zone edges are superimposed on the surface corresponding to 0% strain. 60
3.15 Phonon frequencies as a function of strain for [111] tension. 61

4.1 Linear thermal expansion coefficient of Ta as a function of temperature from experiment (open symbols) [70] and computed within the quasi-harmonic approximation (filled symbols). 66

List of Tables

2.1 Lattice parameters, volumes, relative energies and elastic constants of Fe from PAW and FLAPW calculations as well as experiment. All energies are relative to the FM bcc phase which is taken as 0. Experimental elastic constants at 4K are from [44] and the experimental lattice parameter extrapolated to 4 K is from [45]. 18

2.2 Summary of symmetries, stresses, and strains associated with instabilities and saddle points. For tension, the strains are referred to a bct cell with the unique [001] axis along the z-axis. For <111>{112} shear, the reference structure is a base centered monoclinic cell with its 2-fold axis parallel to the x-axis, one orthogonal lattice vector parallel to the the shear direction which coincides with the y-axis, and the other orthogonal lattice vector in the y-z plane. For <111>{110} shear, the reference structure is a triclinic cell with one lattice vector in the shear direction which coincides with the y-axis, the second lattice vector in the shear plane which coincides with the x-y plane, and third vector with some component in the z-direction. 27

3.1 Lattice parameter and elastic constants of fcc Al from theory and experiment. Experimental lattice parameter was extrapolated to 4K using low temperature thermal expansion data [70]. Experimental elastic constants at 4K are from [71]. 40

3.2 Ideal strengths of Al and Cu for <110> tension, <001> compression, and <112>(111) shear as well as the maximum resolved shear stress acting on the <112>(111) shear system for each loading configuration. 46

3.3 Stresses and strains associated with phonon instabilities as compared to the elastic instabilities in the same direction. Also shown are the shear plane and displacement associated with the phonon instabilities. 54

Acknowledgments

Portions of the material presented in this dissertation have previously been published or submitted for publication in the technical literature. These articles have been coauthored with J. W. Morris Jr., D. C. Chrzan, C. R. Krenn, and M. L. Cohen. I gratefully acknowledge their permission to reproduce some of this coauthored work in this dissertation.

The research presented in this dissertation was supported by the Director, Office of Energy Research, Office of Basic Energy Sciences, Materials Sciences Division of the US Department of Energy under Contract No. DE-AC03-76SF00098. Portions of this work were also performed under the auspices of the US Department of Energy by the University of California, Lawrence Livermore National Laboratory, under Contract No. W-7405-Eng-48. Supplemental computational resources were provided by the National Energy Research Scientific Computing Center which is supported by the Director, Office of Science, Division of Mathematical, Information, and Computational Sciences of the US Department of Energy under Contract No. DE-AC03-76SF00098.

Chapter 1

The Ideal Strength

The field of computational materials science has grown rapidly over the past decade. Development in the field has been catalyzed by progress in two main areas. First, the availability of powerful computing machines has grown dramatically as the associated processor performance has essentially doubled every 1.5 years. The second area of improvement relates to the necessary theoretical tools. Refinements have been made to density functional theory (for example, the generalized gradient approximation) leading to increased accuracy. Experience has also produced a better understanding of the limits of the theory. Associated with these advances in the theory, new methods for determining the density functional ground state charge density have been developed as have improvements in the algorithms needed to carry out these calculations.

As a result of these advances, the prediction of materials properties from first principles has become increasingly widespread and has produced many notable successes. For example, the structural (crystallographic) properties predicted by the theory are often found to agree with the associated experimental values to within 1%. The fastest developments have occurred in calculating properties which are not highly sensitive to structural defects and thus can be determined from computations on perfect crystals. Such properties include the elastic constants of a material, and the magnetic moment per atom. With advanced theoretical tools one can also make good progress in understanding the electrical, and optical properties from first principles. However, properties that are highly are sensitive to structural defects, such as the yield strength of metal, have posed a greater challenge to researchers.

The difficulty essentially arises from the large number of atoms needed to study the effect of defects on the property of interest. For example, the yield strength depends on

the interaction of a large number of dislocations which interact over distances on the order of microns. As such, performing a brute force molecular dynamics calculation would require following the motion of $\sim 10^{15}$ atoms for a minimum of 1 second. Unfortunately, the current state of the art electronic structure methods can compute the trajectory of $\sim$1000 atoms for a few pico-seconds. Obviously the gap between what is desired and what is achievable is unmanageably large. An alternate to this brute force approach is the use of multi-scale modeling. This concept requires that calculations be performed at various scales spatially and temporally with the aggregate results at each level used as input into models at the next larger scale. The main barrier to employing this method is the need to pass information from level to level: one must aggregate the results of the calculation at each step while at the same time not loosing any of the "important" information. Additionally, one must ensure that the models at larger length scales contain sufficient physics in order to model the processes of interest.

It is obvious from the above discussion that we cannot use *ab initio* methods to directly solve all of the problems in the area of mechanical properties. However, there are an number of problems within this area which are well defined and can be solved exactly from first principles. Thus, a logical starting point for building an understanding of the mechanical properties of materials from an atomistic standpoint is to explore these problems in detail. The results of these studies will hopefully lead to insights which can then be used to extend the theory to broader classes of problems. It is also possible that the results of these calculations can be used as input parameters in other larger scale models. Examples of problems which can be solved exactly from first principles include the elastic constants of a material, the core structure of dislocations, as well as the energy of stacking faults. Another important mechanical property that can be studied directly using *ab initio* methods is the topic of this thesis – the ideal strength.

1.1 Relevance of the ideal strength

The ideal strength of a material can be defined as the stress required to cause a perfect defect-free crystal to become mechanically unstable [1]. Many simple models for the ideal strength have been developed over the past 80 years, notably those of Frenkel [2] and Orowon [3]. These have proven to be convenient means of understanding this topic; however, recent advances have made it possible to study the ideal strength quantitatively and in greater detail using *ab initio* electronic structure calculations [4-9].

While crystalline materials are normally deformed or broken by defects that become active at stresses well below the ideal strength, the ideal strength is interesting and important for several reasons [7]. First, it is an inherent property of the crystal lattice and, thus, offers insight into the connection between the intrinsic bonding and symmetry of the crystal and the mechanical properties it displays. In fact, many of the familiar aspects of the mechanical behavior of crystalline solids, such as the {100} cleavage of bcc crystals, the cleavage resistance of fcc materials, and the common slip systems of fcc and bcc are some inherent features of behavior at the limit of strength [10].

Second, the ideal strength is an inherent upper bound on the strength. While the mechanical properties in general are known to depend on a material's microstructure and defects, there is no modification of the microstructure which will allow one to exceed the ideal strength. The ideal strength is useful to know since it sets clear limits on the attainable mechanical properties. For example, the ideal strength suggests a practical upper bound on the yield strength of ductile steel, and suggests why Ni additions may promote ductile fracture in high strength steel [11].

Third, as is becoming increasingly evident, the ideal strength is actually approached in a number of practical situations. Since a material will fail at a stress needed to produce deformation by the easiest mechanism, the ideal strength will only be reached in situations in which other mechanism are inhibited such as when there are few mobile defects. The best quantitative data demonstrating the possibility of approaching the ideal strength experimentally comes from the nanoindentation of materials with low defect densities [12]. In this situation a diamond indenter with a tip radius of on the order of 50 nm is pressed into the polished surface of a material. Because of the small size of the indenter, it is possible for the area influenced by the imposed stress field to be defect free. Also, because the maximum stresses in the test occurs below the surface, the nucleation of dislocations from the free surfaces is inhibited. During nanoindentation, the material deforms elastically until a critical load at which the material suddenly deforms plastically. The elastic nature of the initial deformation suggests that in this region the movement of defects does not play an important role and thus the ideal strength may be relevant. In fact, using a combination combination of first-principles electronic structure calculations and finite element modeling Krenn et al. have demonstrated that the maximum stresses extracted from an analysis of experimental nanoindentation data are within 10% of the calculated ideal strength [12].

We also expect the ideal strength to be approached in inherently hard materials in which the Peierls barrier is of the same magnitude as the ideal strength. This is simply

a restatement of the fact that the strength will be set my the weakest deformation mechanism. Another experimental situation allowing one to approach the ideal strength is the deformation of materials at extremely high strain rates. If a material is forced to deform at rates higher than can not be accommodated by motion of dislocations (due to their finite mobility), the failure criterion might be set by the ideal strength.

Finally, the ideal strength is important because it is one of the few mechanical properties of materials that can be computed from first principles. As mentioned earlier, this puts the ideal strength in special class of mechanical properties which can form a foundation for building an understanding the mechanical properties of materials from the atomistic level.

1.2 Phase transformations and the ideal strength

While one does not often associate the study of phase transformations with the deformation and fracture of materials, there are several reasons why one might do so [7]. A solid that is subject to a deviatoric stress is always at least metastable with respect to transformation into a state that is free of of this deviatoric stress [13]. This transformation can result in a deformed (sheared) replica of the original phase, a set of fractured stress-free pieces, or a new crystal structure. As is the case for most phase transformations, this process can occur by heterogeneous nucleation, homogeneous nucleation, or as the result of a thermodynamic instability. In most materials, deformation is nucleated heterogeneously at defects in the structure (i.e. fracture initiated at a pre-existing crack, dislocation slip originating at a surface); however, in the absence of defects the material will fail when the stress is sufficient to homogeneously nucleate structural defects or to cause the crystal lattice itself to become unstable.

The mechanical instability of the crystal lattice defines the ideal strength. However, at a more fundamental level, this mechanical instability may itself be the result of some other type of phase transformation in the form of a thermodynamic instability. As an example, we note the stress induced martensitic transformation found in some austentic steels and "memory metal". Another example arises in Chapter 2 of this thesis. It is shown there that iron can undergo an stress induced magnetic instability which can trigger a mechanical instability. Ferroelectric as well as metal-insulator transformations have also been found to limit the ideal strength in TiN and HfC [14]. Although the author is not aware of any examples in which second order order-disorder transformations or spinodal (compositional)

instabilities trigger a mechanical instability, it does not appear that there is any fundamental reason why this situation could not arise provided the necessary symmetry requirements are obeyed.

We can further classify the mechanical instability as being associated with vibrational modes (a phonon instability) or with homogeneous deformation (an elastic instability). The latter has been much more extensively discussed in the literature and has been the focus of most studies on the ideal strength. While the concept of an elastic instability is somewhat straight forward – a spontaneous homogeneous deformation – the precise definition contains some subtle features. Of course, the strength associated with an elastic instability depends on the geometry of the load; the strength in tension depends on the direction of the tension, the strength in shear on the plane and direction of shear, the strength under multiaxial loading on the geometry of the multiaxial load. But the load that induces instability in an actual test may also depend on the response of the loading mechanism [15, 16]. In this case the measured value of the limiting strength is not necessarily a material property. Nonetheless, there is a well-defined inherent value of the ideal strength for any load geometry. It can be found from Gibbs' condition of internal stability: it is necessary (though not sufficient) for mechanical stability that the material be stable with respect to internal rearrangements that leave its boundaries fixed [17]. This condition is satisfied for a strained solid when every possible incremental strain increases the free energy. It has been shown by Morris and Krenn that this requires that the symmetrized Wallace tensor be positive definite. This definition is also equivalent to the failure of a material in a loading mechanism which maintains the Cauchy stress to second order. As the above condition is necessary but not sufficient, a test sample in a loading device may fail at a load below the ideal strength defined by the first vanishing eigenvalue of the symmetrized Wallace tensor, but it must fail when this strength is reached.

The elements of the Wallace tensor incorporate the elastic constants of the crystal in its current state of strain. While it is possible to compute the elastic constants for every step along a hypothetical strain path in an *ab initio* study of elastic stability, it is tedious to do so. And it is usually unnecessary. We are ordinarily interested in the ideal strength for some simple example of the applied stress, such as uniaxial tension or simple shear. In these cases the ideal strength is ordinarily the maximum stress along the "relaxed" loading path in which all stresses orthogonal to the applied stress are zero. The possible exceptions involve instabilities that are orthogonal to the loading direction, such as a hypothetical shear instability that terminates deformation in uniaxial tension. It follows that the ideal

stress can, ordinarily, be found directly by straining the material with the load of interest up to the maximum stress, while periodically applying low symmetry distortions to test for orthogonal instabilities. This procedure is well suited for *ab initio* calculations of the ideal strength [17].

It is also possible for a material to become unstable with respect to vibrational instabilities before the material becomes elastically unstable. In all such cases, the material can lower it energy by introducing a periodic displacement with a non-zero wavevector. This results in negative eigenvalues of the dynamical matrix (or the propagation matrix in the limit of long wavelengths); therefore, stability requires that this matrix be positive definite when evaluated at every wavevector in the Brillouin zone [18].

In the limit that the wavevector of the unstable phonon approaches zero, the material will become unstable with respect to homogeneous deformation and is thus elastically unstable. However, the reverse situation does not appear to be true. It is possible for a material to be elastically unstable while being stable with respect to all long wavelength phonons. For example, there is no long wavelength phonon which is equivalent to producing a uniform dilation Δ. We can see this by computing the strain associated with an arbitrary phonon with displacement vector $\mathbf{w}$ and wavevector $\mathbf{k}$. The displacement $\mathbf{u}$ produced by this phonon at time $t = 0$ is

$$\mathbf{u} = \mathbf{x} - \mathbf{X} = \mathbf{w} \sin\left(\mathbf{k} \cdot \mathbf{X} - \omega t\right) \tag{1.1}$$

$$u_i = w_i \sin\left(\sum_{m=1}^{3} k_m X_m\right), \tag{1.2}$$

where $\mathbf{x}$ are the coordinates of a material in the current state and $\mathbf{X}$ are the coordinates in a reference state. Thus the displacement gradient is found to be

$$\frac{\partial u_i}{\partial X_j} = w_i \cos\left(\mathbf{k} \cdot \mathbf{X}\right) \frac{\partial}{\partial X_j}\left(\sum_{m=1}^{3} k_m X_m\right) \tag{1.3}$$

or

$$u_{ij} = w_i k_j \cos\left(\mathbf{k} \cdot \mathbf{X}\right). \tag{1.4}$$

In the limit of small wavevectors this becomes

$$u_{ij} = w_i k_j = \begin{pmatrix} w_1k_1 & w_1k_2 & w_1k_3 \\ w_2k_1 & w_2k_2 & w_2k_3 \\ w_3k_1 & w_3k_2 & w_3k_3 \end{pmatrix}. \tag{1.5}$$

In order to produce a uniform dilation, u_{12} must be zero. This requires that either w_1 or k_2 be zero; however, if either of these are true this will violate the requirement that $w_1k_1 = w_2k_2 = w_3k_3 = \Delta/3$.[1] In other words, it is not possible to specify a wavevector $\mathbf{k}$ and a displacement vector $\mathbf{u}$ for the phonon such that the resulting strain field is a constant and is isotropic, even if we allow the magnitude of the wavevector to become vanishingly small. It is possible to produce uniform dilation through a linear combination of phonons with different wavevectors and different displacement vectors, but the stability with respect to this dilation can not be tested by examining the stability of each of its component phonons or by examining the eigenvalues of the dynamical matrix at any one point in the Brillouin zone. Based on this analysis, the phonon dispersion can be used to find vibrational instabilities; however, the conditions of elastic stability are more restrictive than the requirement that the slope of the phonon dispersion near the gamma point be positive and real. Thus elastic stability must be tested by either computing the eigenvalues of the Wallace tensor as a function of strain or by applying low symmetry distortions along the loading path as discussed above.

In the following chapters, the principles discussed thus far will be applied to two materials of interest: iron and aluminum. We will explore the ideal strength of these materials and how it is limited by elastic, magnetic, or phonon instabilities.

[1] That this must be true is also obvious given the fact that $u_{ij} = w_i k_j$ is a matrix of rank 1, while a uniform dilation requires that the strain tensor have rank 3.

Chapter 2

Iron: Elastic and Magnetic Instabilities

2.1 Introduction

Iron forms the foundation for some of the most common structural materials of modern times, steels. Thus, understanding the mechanical properties of iron is of great practical interest. In order to pursue this goal, the present research takes the approach discussed in Chapter 1 whereby the ideal strength is used as a basis for studying the mechanical properties. While pure iron is rarely used as a structural material, based on the fact that the elastic properties of materials are not strongly sensitive to small changes in composition, one would expect that the ideal strength of iron should closely approximate that of a large class of steels (low alloy steels, plain carbon steels, etc.), and serve as a rough guide for other steels with higher alloy content.

Although detailed *ab initio* computations of the ideal strength of iron had not been performed prior to the current work[1], the ideal strengths of other bcc metals (W, Mo, Nb) have been published by several investigators [9, 21, 22] and lay a foundation for a study of iron. These results show that symmetry plays a dominant role in determining the ideal strength [7, 6]. The energy of the crystal is a function of the six independent components of the strain and is, hence, a 6-dimensional hypersurface in a 7-dimensional space. The local minima and the saddle points on this hypersurface almost always correspond to structures with high symmetry. The configurations of greatest interest are the saddle points in the energy surface that surround the initial state. The ideal strength is determined by the

[1]Some of the research presented in this chapter has previously been published in Refs. [19, 20].

steepest encountered slope along the path from the initial state to the first saddle point. Thus each elastic instability is associated with a saddle point structure. Four possible saddle point structures have been identified in previous studies of the the ideal strengths of bcc metals: the fcc structure, the simple cubic (sc) structure, a body centered tetragonal (bct), and a base centered orthorhombic structure [21-23]. For example, relaxed shear of a bcc metal in the "easy" <111> direction on the {112} or {110} plane generates a stress-free bct structure [22]. Because the <111>{112} shear system is not symmetric in the sign of the shear direction, it is also possible to move from a bcc structure to a base centered orthorhombic structure by shearing in the "hard" direction. Uniaxial tension in the <111> direction takes a bcc structure to a sc structure [21, 23], while <001> tension moves from bcc to either fcc (the Bain transformation [7]) or the same stress-free bct structure encountered in shear [22]. The competition between the two possible paths that can be reached by <001> tension has the result that, while most bcc crystals (Mo, W) are governed by the instability associated with the fcc structure, some (Nb) become unstable with respect to evolution toward the bct saddle point [22].

Ab initio total energy calculations of the ideal tensile strengths of unconstrained bcc metals show that they are weakest when pulled in a <001> direction [7] (unsurprisingly, {001} is the dominant cleavage plane in bcc metals). As such we will focus on the tensile strength in this direction. A constant volume tensile strain along <001> converts the bcc structure into fcc at an engineering strain of about 0.26 (the 'Bain strain'), see Figure 2.1. By symmetry[2], both structures are unstressed, so the tensile stress must pass through at least one maximum along the transformation path. Following Orowon [3], if we assume a single extremum (the solid line in Figure 2.2) and fit the stress-strain curve with a sinusoid that has the correct modulus at low strain, the ideal tensile strength in <001> is approximately [7, 9]

$$\sigma_m = 0.08 E_{<001>} \tag{2.1}$$

in good agreement with *ab initio* calculations (for example, $\sigma_m = 30$ GPa $= 0.072 E_{<001>}$ for W [9]).

Unfortunately, an obvious problem arises when one considers extending this analysis to iron. The above analysis assumes that the fcc phase is unstable with respect to tensile elongation in the <001> direction, whereas the fcc phase in Fe is known to have an energy only slightly above that of bcc and is at least metastable at low temperature. In fact, the

[2]While magnetism breaks the cubic symmetry of bcc and fcc iron, both structures remain stress free.

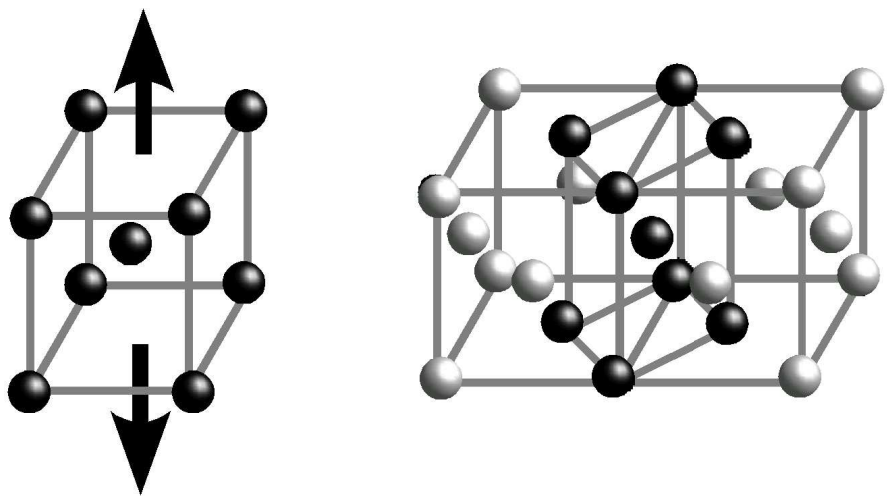

Figure 2.1: The bcc crystal structure becomes the fcc structure after fully relaxed elongation along the <100> direction.

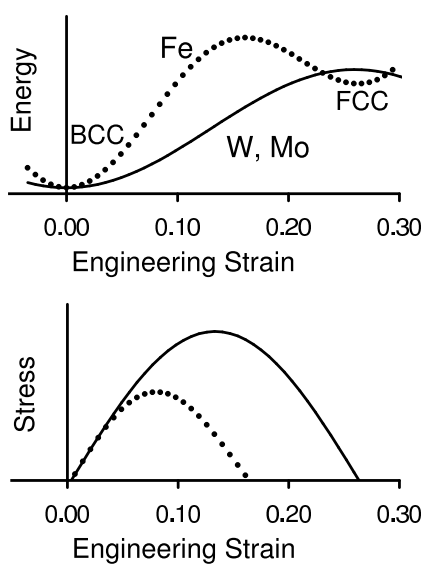

Figure 2.2: The energy as a function of strain has an extremum at the fcc structure which can be a local maximum (solid line) or minimum (dotted line). Assuming sinusoidal form, the inflection point governing the ideal strength falls at a much lower strain in the latter case, and the ideal strength is significantly less.

thermomechanical treatments that are used to process structural steel rely on the ease of transforming it from bcc to fcc and back again [11, 24]. If we assume a metastable fcc phase connected by a continuous strain-energy curve (the dotted line in Figure 2.2), the tensile instability intrudes at a much smaller strain, and the ideal strength should be only about 6 GPa (versus 12 GPa based on an unstable fcc). This number is too small to be credible. Since tensile stresses that are several times the yield strength are developed ahead of crack tips in elastic-plastic materials [11, 25], steels with yield strengths much above 1 GPa would necessarily be brittle. In fact, steels with much larger yield strengths have high fracture toughness and considerable ductility [24].

A possible resolution of this paradox is suggested by the work of Herper et al. [26]. They computed the energy of Fe for various magnetic states and lattice strains. Their calculations suggest that the energy of ferromagnetic Fe increases monotonically if it is distorted toward an unstable, ferromagnetic fcc, which can be stabilized by transforming into a complex antiferromagnetic state. This has the consequence that the low energy antiferromagnetic fcc phase is a minimum rather than a saddle point on the strain-energy surface of Fe. Because the ideal strength is ordinarily determined by the nature and location of the saddle point structures, one might expect that Fe would behave very differently than other bcc metals. In order to better understand the ideal strength of iron and clarify the role played by magnetic instabilities, we have performed a detailed study of the ideal strength of iron.

2.2 Computational methods

Computationally, the non-local magnetic interactions in Fe have the consequence that *ab initio* computational methods that employ the local density approximation cannot be used. In fact, the local density approximation predicts that the ground state of Fe should be a non-magnetic close packed structure rather than a bcc ferromagnet. The use of the generalized gradient approximation (GGA) has been shown to correct this problem [27]. However, these results suggest that the energy differences between various phases are due to subtle differences in their charge density and charge density gradients. Full Potential Linearized Augmented Plane Wave (FLAPW) calculations which make no further approximations beyond the GGA (assuming convergence of the basis set, charge density representation and Brillouin zone integration) are probably the most reliable [28]. Unfortunately, in order to efficiently relax the stresses orthogonal to the applied stress, the stresses on the unit cell must

be directly computable, and there are no implementations of the FLAPW method known to us which can compute stresses via the Hellmann-Feynman theorem. For the current work we report the results from the Projector Augmented Wave (PAW) method, originally developed by Blöchl [29]. We have also performed some calculations using the FLAPW method and provide these results when available for comparison and as a check on the accuracy of the calculations. As we shall show below, the two methods show reasonable agreement which adds confidence to the reliability of the calculations.

All computations have been carried out within the framework of density functional theory [30, 31] within the generalized gradient approximation (GGA). For PAW method calculations, we used the implementation provided within the Vienna Ab-initio Simulation Package (VASP) [32-34]. This code uses a somewhat non-standard exchange correlation functional. The local density part of the exchange correlation energy was taken from the Perdew and Zunger [35] parameterization of the Ceperly and Alder [36] quantum Monte Carlo calculations, and adopted the Vosko-Wilk-Nusair (VWN) [37] spin interpolation of the local correlation energy. The gradient corrections of Perdew and Wang (PW92) [38, 39] were used with the exception that the correlation part of the GGA was interpolated from the non-magnetic to the magnetic regime using the standard interpolation instead of the VWN interpolation formula. We used a scalar relativistic treatment for the 3d and 4s valence states, while treating the lower energy levels with the frozen core approximation. The plane-wave expansion had an energy cutoff of 25 Ry. We employed the modified tetrahedron method of Blöchl [40] for integration in the Brillouin zone, with the number of k-points dependent on the structure and number of atoms per unit cell in order to converge the energy to within 0.1 mRy and the Hellmann-Feynman stresses to within 0.1 GPa based on convergence studies. In general a 17x17x17 Monkhorst Pack Grid [41] was sufficient; however, some calculations were done with a more dense mesh of k-points. The stresses for several structures were also compared to calculations which used the integration scheme of Methfessel-Paxton [42] and were found to agree within 2%.

FLAPW calculations were performed using WIEN97 [43] with the GGA parameterization described by Perdew et al. [38]. The [Ne] $3s^2$ states were treated as core states using the relativistic Dirac equation, while $3p^6 3d^6 4s^2$ states were treated as valence states using the scalar-relativistic approximation. We also included "local orbitals" for the 3d and 3p states to increase the flexibility of the basis set and reduce linearization errors [28]. The radius of the "muffin tin" was 2.0 au, with 781 radial mesh points. Our basis cutoff was $R_{mt} \bullet K_{max}$=10 and the charge density was expanded up to G_{max}=14 $Ry^{1/2}$. We used the

modified tetrahedron integration method of Blöchl et al. [40] with between 196 and 286 k-points in the irreducible wedge of the Brillouin zone, depending on the particular crystal structure. The total errors, stemming from the choice of basis set, Brillouin zone sampling, and neglect of spin-orbit coupling[3] are of the order of 0.1 mRy/atom.

The ideal strength was computed for uniaxial stress in tension or shear. The lattice vectors were incrementally deformed in the direction of the imposed stress, and at each step the structure was relaxed until the stresses orthogonal to the applied stress vanished, as indicated by those components of the Hellmann-Feynman stresses being less than 0.15 GPa [8]. Because there is no unique measure of strain for a given finite deformation, we describe our deformations in terms of the engineering strain from the equilibrium structure. The initial set of lattice vectors $\mathbf{r}^{\alpha}(\alpha = 1,2,3)$ in an orthogonal coordinate system become the vectors $\mathbf{r}^{\alpha'}$ after homogeneous deformation by the transformation $r_i^{\alpha'} = r_i^{\alpha} + D_{ij} r_j^{\alpha}$. From this transformation, we define the strain to be $e_{ij} = \frac{1}{2}[D_{ij} + D_{ji}]$. As is customary, we redefine the shear strains to be $\gamma_{ij} = 2e_{ij}$ for $i \neq j$. While the engineering strain is convenient for describing the change in the lattice vectors from their original configuration, the Cauchy (true) stress cannot be calculated from the derivative of the free energy with respect to this strain measure. To compute the Cauchy stress we take the derivative of the free energy with respect to the incremental strain from a nearby reference state, yielding a stress that converges to the thermodynamic definition of the Cauchy stress in the limit of small incremental strain.

It should be noted that the ideal strengths determined from these calculations are for quasi-static deformation at 0K, and that other dynamic instabilities such as soft phonons may lower the ideal strength.

2.3 Equilibrium structures

We chose to compute the ideal strength with the Projector Augmented Wave (PAW) method because of its computational efficiency and its ability to treat lattice stress. To check the accuracy of the method, we computed the energy as a function of volume for several magnetic structures and compared the results to calculations done using the FLAPW method as well as with available experimental data. The magnetic structures included the following: bcc ferromagnet (FM), fcc ferromagnet (FM), fcc antiferromagnet (AFM), fcc

[3]While the total energy is lowered by approximately 0.5 mRy/atom when the spin-orbit interaction is included using the second-variational procedure [28], the energy difference between the equilibrium bcc phase and the bct phase at the point of elastic instability is changed by only ~0.12 mRy/atom.

non-magnetic (NM). The results are shown graphically in Figure 2.3 and 2.4, while the equilibrium volumes, bulk moduli, and relative cohesive energies are compared in Table 2.1.

In general the agreement between the two methods is good. In comparing the PAW and FLAPW methods we find that the equilibrium volumes of the various phases agree to within 1%. The elastic constants of the bcc FM phase agree to within 3% with the exception of c_{44} which has a discrepancy of 13%. The agreement in the energy differences between the various magnetic phases is not quite as good with errors ranging from 3-16%; however, these differences are probably of the same magnitude as the errors the generalized gradient approximation introduces as compared to the true density functional groundstate. In comparing the PAW potential used in this study with independent FLAPW calculations, Kresse and Joubert [34] found that there was a 12% discrepancy in the energy difference between the fcc NM and bcc FM phases (using GGA), of the same order as the error reported here. We also note that the calculations used slightly different representations of the exchange correlation energy; however, both representations are roughly based on PW92 [38].

Compared with experimental measurements of the bcc phase at 4 K, the PAW calculations predict a lattice parameter that is too small by 1% [44] and elastic constants which are generally about 10% too large [45] suggesting a slight over-binding (the only discrepancy being c_{44} which is 18% too small). From the computed elastic constants, the relaxed tensile modulus in the <001> direction, $E_{<001>} = 1/s_{11}$, is found to be about 29% too large, while the relaxed shear modulus in the <111> direction, $G_{<111>} = \frac{3c_{44}(c_{11}-c_{22})}{4c_{44}+c_{11}-c_{12}}$, is about 18% too large.

In regards to the magnetic properties, both the PAW and FLAPW methods correctly predict that the ground state is the bcc ferromagnetic phase with a magnetic moment of 2.20 μ_B and 2.15 μ_B respectively as compared to the experimental value of 2.22 μ_B [46]. Both sets of calculations also predict that the ferromagnetic fcc phase undergoes pressure induced first order phase transformation at a volume of 76-77 au^3/atom from a low-volume, low-moment phase to a high-volume, high-moment phase. The groundstate magnetic structure of fcc Fe has been debated on theoretical grounds extensively in the literature [47-51]. While bulk fcc Fe is difficult to achieve experimentally at low temperature, there is some probative experimental data on the magnetic state of nearly pure Fe in the fcc crystal structure. It is possible to stabilize fcc Fe by growth as a thin epitaxial film or as small precipitates in a copper matrix. Tsunoda [52, 53] found that small fcc precipitates in Cu that are almost pure Fe have a spiral spin density wave (SSDW) ground state. Knöpfle et al. [47] have

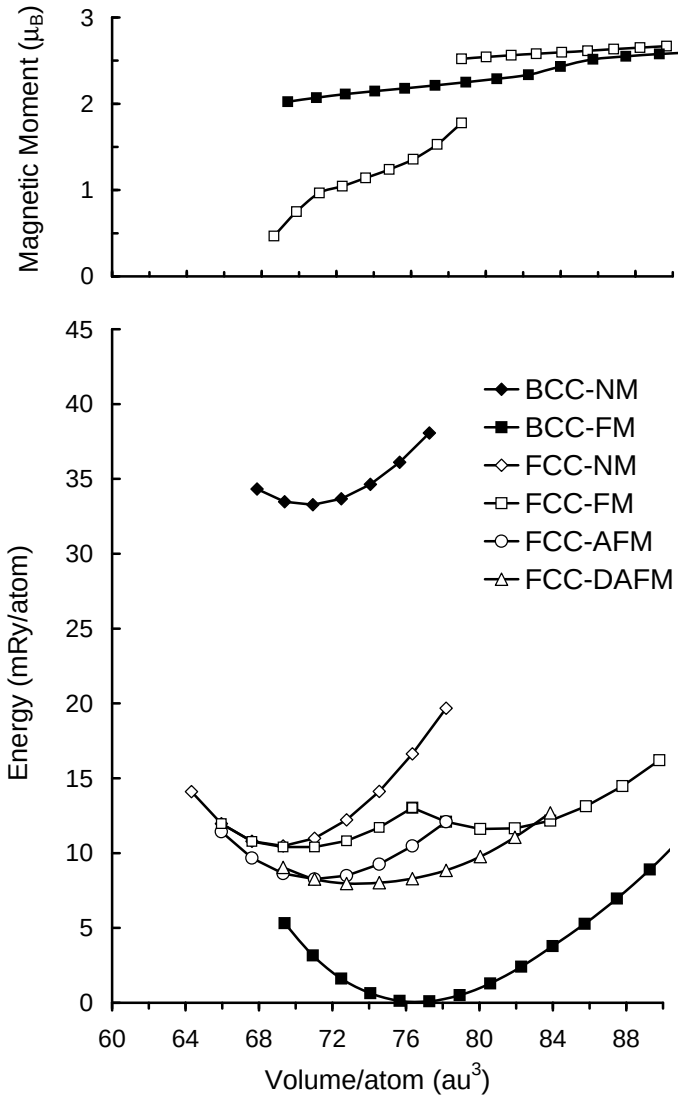

Figure 2.3: The energy and magnetic moment per atom as functions of volume computed using the PAW method for Fe in the bcc (filled symbols) and fcc (open symbols) crystal structures for several magnetic states: (diamonds) non-magnetic (NM), (squares) ferromagnetic (FM), (circles) antiferromagnetic (AFM), and (triangles) double period antiferromagnetic (DAFM). The discontinuity in the fcc FM curve separates two distinct phases with different magnetic moments.

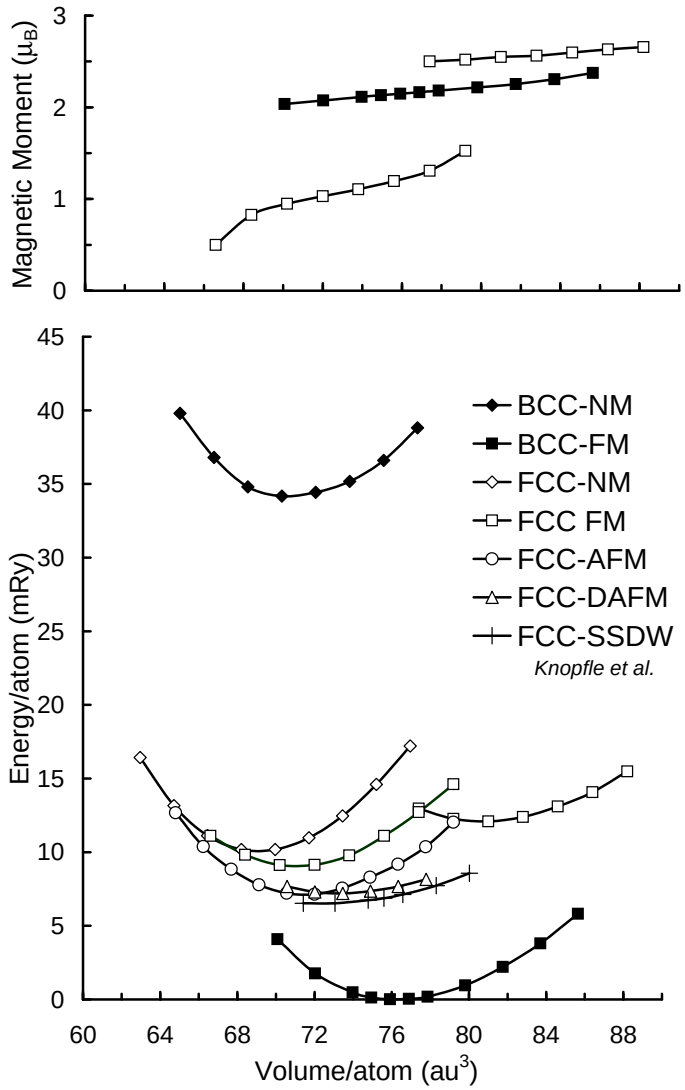

Figure 2.4: The energy and magnetic moment per atom as functions of volume computing using the FLAPW method for Fe in the bcc (filled symbols) and fcc (open symbols) crystal structures for several magnetic states: (diamonds) non-magnetic (NM), (squares) ferromagnetic (FM), (circles) antiferromagnetic (AFM), and (triangles) double period antiferromagnetic (DAFM). The discontinuity in the fcc FM curve separates two distinct phases with different magnetic moments. The energy-volume relation for the ground state spiral spin density wave of fcc Fe [47] is indicated by the points labeled (+). These are plotted relative to the minimum in the AFM curve to correct for a small, consistent difference in the energies calculated by Knöpfle et al. [47].

	PAW	FLAPW	PAW-FLAPW % Error	Experiment (4K)	PAW-Experiment % Error
bcc-FM					
V_o au^3	76.47	76.20	0.4%	78.94	-3.1%
a_o (Å)	2.830	2.827	0.1%	2.86	-1.1%
B (GPa)	194	196	-1.0%	174	11.5%
c_{11} (GPa)	286	289	-0.9%	245	16.9%
c_{12} (GPa)	147	152	-3.43%	139	5.9%
c_{44} (GPa)	99	114	-12.8%	122	-18.5%
$E_{<001>}$ (GPa)	187	184	1.5%	144	29.2%
$G_{<111>}$ (GPa)	77	78.9	-1.9%	65	18.4%
μ (μ_B)	2.2	2.15	2.3%	2.22	-1.0%
fcc-AFM					
V_o au^3	71.19	71.50	-0.4%		
B (GPa)	202	209	-3.6%		
E_c (mRy)	8.2	7.1	15.7%		
fcc-FM					
V_o au^3	80.81	80.7	0.1%		
B (GPa)	160	168.6	-5.3%		
E_c (mRy)	11.5	12.0	-4.2%		
fcc-LSFM					
V_o au^3	70.10	70.88	-1.1%		
B (GPa)	171	207	-17.1%		
E_c (mRy)	10.2	9.0	13.7%		
fcc-NM					
V_o au^3	69.06	69.09	-0.04%		
B (GPa)	284	286	-0.8%		
E_c (mRy)	10.5	10.1	3.8%		

Table 2.1: Lattice parameters, volumes, relative energies and elastic constants of Fe from PAW and FLAPW calculations as well as experiment. All energies are relative to the FM bcc phase which is taken as 0. Experimental elastic constants at 4K are from [44] and the experimental lattice parameter extrapolated to 4 K is from [45].

recently published calculations using the modified augmented spherical wave method which show good agreement with this experimental data. Their minimum energy fcc structure has a spiral vector of $\mathbf{q} = (0.15, 0, 1)$ with an energy which lies <1 mRy below the AFM phase and has a slightly larger equilibrium volume than the AFM phase. The results of their study are included in Figure 2.4 where we have plotted the energy as a function of volume for the SSDW relative to the minimum in the AFM curve to correct for a small, consistent difference in the energies calculate by Knöpfle et al. [47].

Due to the complexity involved in treating non-collinear magnetism, in the present work we have used collinear structures as approximate representations of the true magnetic ground state. Herper, Hoffmann, and Entel [26] proposed using a collinear double period antiferromagnetic structure (DAFM) as an approximate to the non-collinear ground state in fcc Fe. In this structure the spins on (002) planes are oriented up-up-down-down. The energy as a function of volume of this structure is plotted in Figure 2.4 and we see that it is located <1 mRy below the AFM phase and has a similar equilibrium volume. The proximity of this phase to the SSDW curve in the plot suggests that the DAFM structure may be a good approximate to the non-collinear fcc structure.

As a further check on the accuracy of the PAW method, some of the ideal strength calculations have been verified by comparing the energies computed with the FLAPW and PAW methods for structures which were relaxed using the PAW method. These results are described below where applicable.

2.4 Ideal strength in tension

First consider the ideal strength in tension. Since previous calculations and symmetry arguments suggest <001> is the weakest direction in tension for bcc metals [7], we have focused on the ideal strength in this direction. Figure 2.5 shows the energy and stress as a function of strain for FM Fe.

2.4.1 Tetragonal versus orthorhombic instability

There are two possible deformation paths for uniaxial tension in the <001> direction. An infinitesimal strain in the <001> direction distorts the crystal into a body centered tetragonal (bct) configuration. If we require that the structure maintain tetragonal symmetry, we find that at 28.6% strain the energy reaches a local maxima at the fcc structure (c/a ratio = $\sqrt{2}$), and then at 42% strain it reaches a local minima corresponding to a special

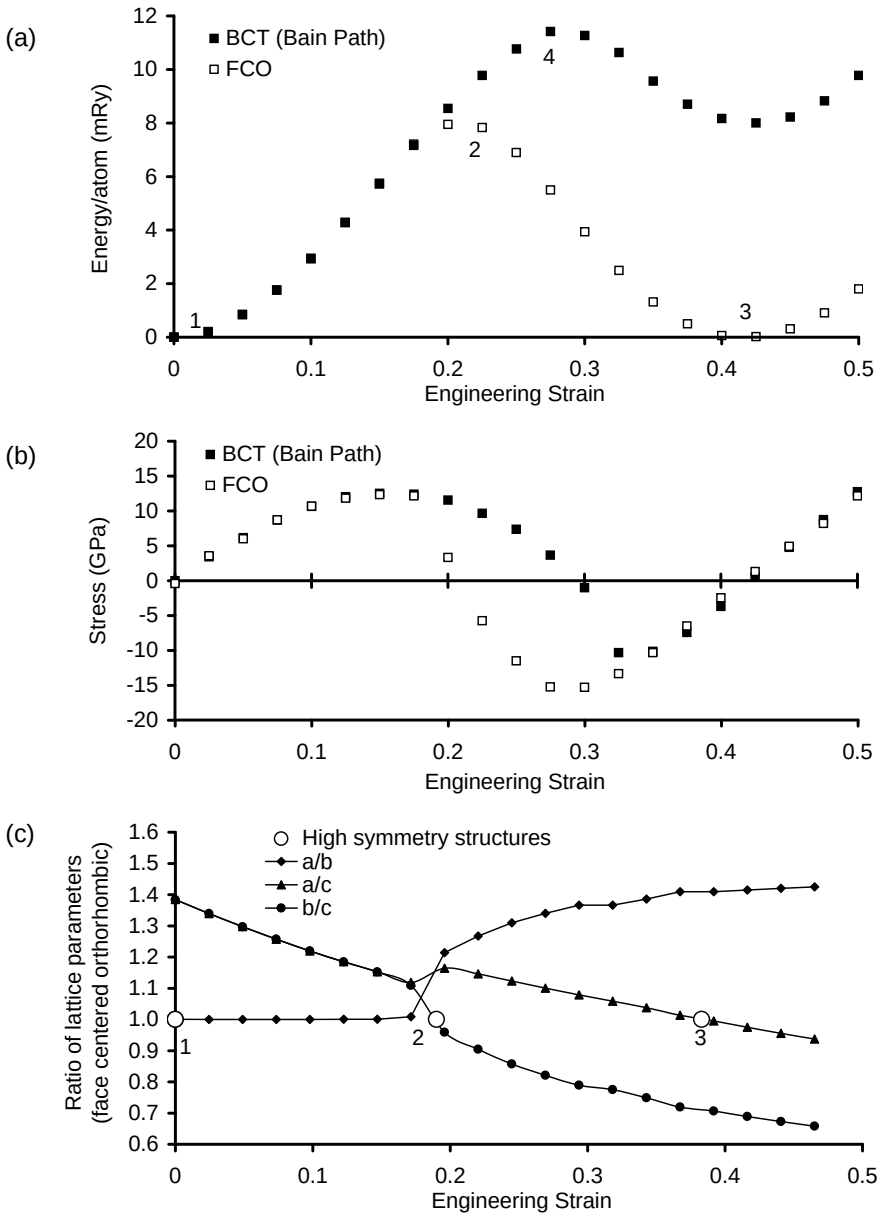

Figure 2.5: (a) Energy and (b) stress as a function of applied tensile strain along <001>: (filled squares) Bain Path with tetragonal symmetry, (open square) orthorhombic path. (c) Ratios of the lattice parameters along the orthorhombic path: (filled diamond) a/b, (filled triangle) a/c, (filled circle) b/c. Numbers and open circles an (a) and (c) indicate special structures with high symmetry that are shown schematically in Figure 2.6.

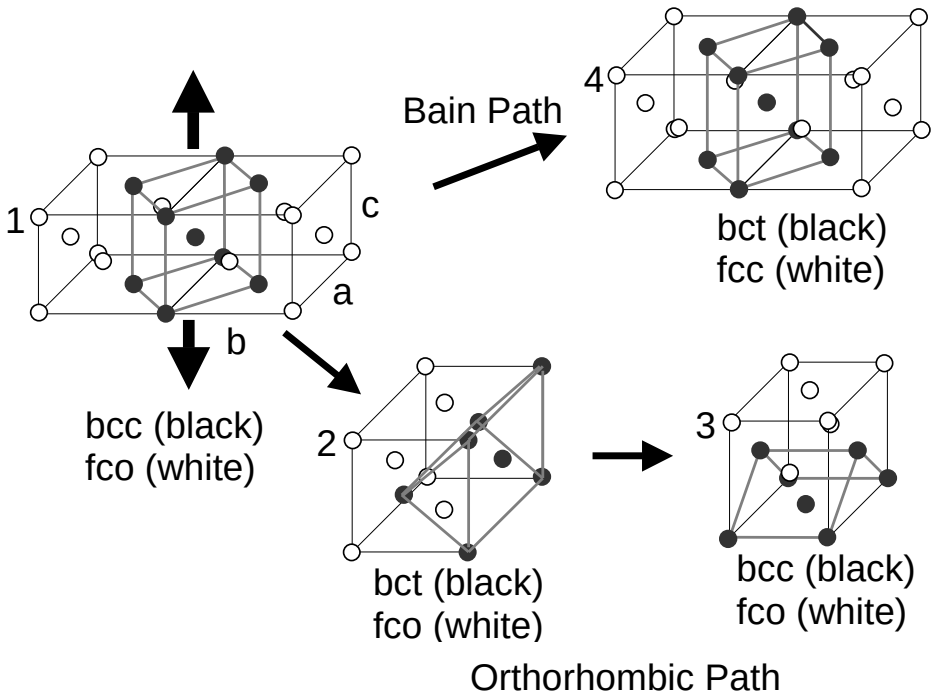

Figure 2.6: The geometry of the Bain path and the orthorhombic instability. The crystal starts as a bcc structure (1) which can also be visualized as a fco structure with a:b:c ratio of $\sqrt{2} : \sqrt{2} : 1$. If tetragonal symmetry is maintained the Bain path is followed to the fcc structure (4) which is equivalent to a bct structure with a c/a ratio of $\sqrt{2}$. If the tetragonal symmetry is broken the orthorhombic path is followed and a maximum energy is reached at a special bct structure (2) which has a c/a ratio of 1.66. From that energy maxima, the orthorhombic path leads down in energy to a bcc structure (3) which is rotated relative to the starting bcc structure.

stress-free bct structure with a c/a ratio of 1.66 (see Figure 2.6). The plot of stress versus strain associated with this path has a maximum tensile stress of 12.6 GPa at 15% strain. The maximum locates the elastic instability associated with the bcc-fcc (Bain) deformation path and corresponds, physically, to cleavage on the {001} plane.

The initial bct structure can also be treated as a special case of a face centered orthorhombic (fco) structure that is rotated by 45° (see Figure 2.6) and has a:b:c ratio of $\sqrt{2} : \sqrt{2} : 1$, where we take the c-axis to lie in the direction of the applied strain. If we preserve orthorhombic symmetry (which allows the tetragonal symmetry to be broken) the deformation is coincident with the Bain path up to a strain of ~18%, but then diverges from it. The evolution of the ratios of the orthorhombic lattice parameters along the loading path is shown at the bottom of Figure 2.5 and the geometric relationship between the special crystal structures is shown in Figure 2.6. At a strain of 18% the crystal becomes unstable

with respect to an orthorhombic distortion. The energy reaches a maxima at 21% strain, then falls off into a local minimum at a strain of 42%. The energy maximum along the orthorhombic path occurs at the "special" bct structure with a c/a ratio of 1.66, and the energy minimum is a bcc structure that is rotated relative to the initial bcc structure (see Figure 2.6). If one refers the structure back to the bct structure with the deformation in the [001] direction, the orthorhombic instability corresponds to the elastic constant c_{66} vanishing leading the crystal to become unstable with respect to a shear, τ_{xy}. Although the crystal is pulled in tension this instability would correspond to a shear failure on the <111>{112} system of the bcc crystal.

The competition between tetragonal and orthorhombic instabilities in bcc crystals was first noted by Luo, et al. [22], who found that the tetragonal instability dominates in Mo (as in W) while the orthorhombic instability intrudes in Nb. The issue is physically important, since the tetragonal instability leads to failure in tension ({001} cleavage) while the orthorhombic instability leads to failure in shear (<111>{112} shear). Fe behaves like the conventional bcc metals, W and Mo. Its ideal strength in <001> tension is determined by the tetragonal instability and, hence, by cleavage on {001}. In keeping with this result, Fe cleaves on {001} when tested at low temperature.

We also computed the ideal tensile strength of Fe using the FLAPW method; however, in those calculations only tetragonal structures were considered. A slightly higher ideal strength of 14.2 GPa was found, which is consistent with the larger energy difference between the bcc FM and fcc FM structures found with the FLAPW method as compared to the PAW method (see Table 2.1). The energy difference may be due to the differences in the treatment of the GGA or errors introduced by the PAW potential. The conditions of stability developed by Morris and Krenn [17] were tested at 14% strain to check for orthogonal instabilities. No orthogonal instabilities were found at that strain, consistent with the PAW calculations. However, the elastic constant c_{66} was found to be only ~30 GPa, quite a bit smaller than in bcc Fe (114 GPa), which is an indication of the close proximity of the orthorhombic instability.

Following Orowon [3], we can model the ideal strength by assuming that the stress strain curve is sinusoidal with an amplitude of σ_m and a period that is twice the strain needed to reach the fcc phase (2x0.286):

$$\sigma = \sigma_m \sin\left(\frac{e\pi}{0.286}\right). \tag{2.2}$$

Requiring that Hooke's law be satisfied for small strains, one finds that:

$$\sigma_m = \frac{0.286}{\pi} E_{<001>} = 0.091 E_{<001>}, \tag{2.3}$$

where $E_{<001>}$ is Young's modulus for elongation in the $<001>$ direction. Equation 2.3 agrees well with the results calculated here: $\sigma_m/E = 0.087$ when the the experimental value for $E_{<001>}$ is used, or $\sigma_m/E = 0.068$ when the calculated value of $E_{<001>}$is used.

2.4.2 Magnetic instabilities

The results to this point have only considered ferromagnetic (FM) states; however, the fact that Fe has a metastable, antiferromagnetic fcc phase at low temperature suggests that it must become unstable with respect to magnetic transitions at large strains. We will now consider this possibility.

For computational simplicity we approximate the magnetic structures of fcc Fe by collinear structures, even though it is fairly well accepted that the ground-state magnetic structures may be complex (such as spin spirals) [47]. It is enormously difficult to treat non-collinear structures. In addition to the problems associated with computing the ground state magnetic structure, one must also ensure that it has the correct stress state. In the computational approach used here we fix the directions of the magnetic moments and relax the lattice into the required stress state. We then increment the strain to obtain the energy and stress as a function of the strain relaxing the lattice at every step along the path. This entire process is then repeated for various magnetic structures. Increasing the degrees of freedom in the magnetic structure significantly increases the number of magnetic structures that must be tested and structurally relaxed. The inclusion of non-collinear structures dramatically increases the number of magnetic degrees of freedom, and is simply impractical with available computational resources. In addition to assuming collinear structures, we used a scalar relativistic approximation that does not include effects of spin-orbit coupling. However, our earlier calculations using the FLAPW method showed that this makes a negligible effect on the energy differences between various magnetic structures. As discussed in Section 2.3, the ability of collinear magnetic structures to mimic the more complex non-collinear structures has been tested for fcc Fe. Based on this success, there is some indication that collinear structures can provide a good approximation.

In Figure 2.7 we present the energy as a function of strain for Fe in the FM, AFM, DAFM and low-spin FM structures. We have studied both bct and fco structures and found that the AFM and LSFM structures remain tetragonal while the DAFM and FM structures

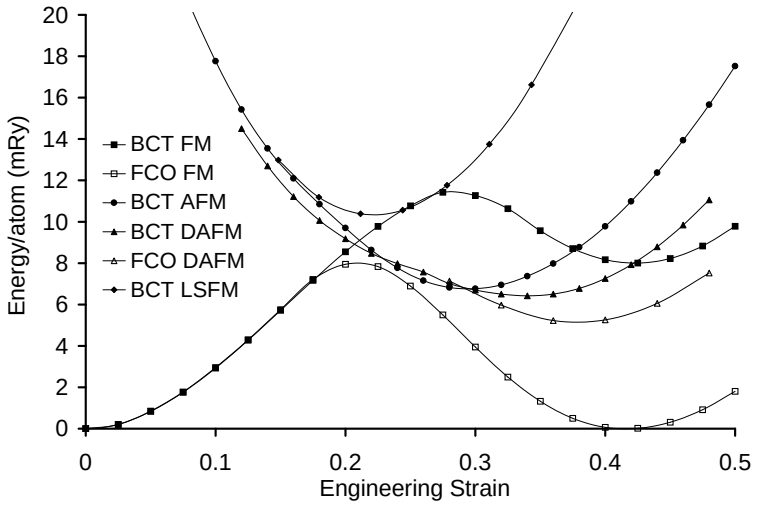

Figure 2.7: Energy versus strain in the <001> direction for various magnetic structures: (solid square) bct-FM, (open square) fco-FM, (filled triangle) bct-DAFM, (open triangle) fco-DAFM, (filled circle) bct-AFM, (filled diamond) bct-LSFM. The fco-AFM and fco-LSFM structures follow paths identical to bct-AFM and bct-LSFM respectively and are not shown. A magnetic phase transformation is seen near 20% strain. Lines are guides for the eye.

undergo a transformation to the fco structure at different points along the loading path. We also see that FM Fe becomes magnetically unstable at about ∼20% strain at which point the DAFM structure is preferred. This result suggests that the ideal strength is not compromised by the magnetic instability since the structural instability ({001} cleavage) is encountered before the magnetic instability is reached. Thus, the ideal strength in <001> tension is 12.6 GPa and is set by a tensile elastic instability along the Bain path from bcc to fcc. The stability of fcc iron is made possible by a magnetic phase transition at larger strains which does not affect the ideal strength.

2.4.3 Comparison with previous calculations and experiment

Several previous authors have studied the energy as function of tetragonality for Fe, but have not determined the ideal strength [26, 54]. Friák et al. [55] have calculated the ideal tensile strength along the tetragonal loading path using the FLAPW method and found a strength of 12.7 GPa in good agreement with our results from the PAW method and slightly lower than our calculations using the FLAPW method (14.2 GPa). While the use of different GGA formulations in the three cases makes exact comparison difficult, the

differences are within the error range for density functional methods. To our knowledge, the only attempt to measure the ideal tensile strength of Fe was by Brenner [56] who tested Fe whiskers in tension. He measured a value of ~5 GPa for tension in the <001> direction [56]. While this value is considerably lower than the calculated ideal strength, the failure initiated at the surface and, therefore, does not represent bulk strength. The measured value of the strength in the <111> direction was 13 GPa, but it is expected that the ideal strength of bcc metals in the <111> direction is significantly larger than in the <001> direction [7, 21].

2.5 Ideal strength in shear

2.5.1 Shear strength of FM bcc Fe

We computed the ideal shear strength for two common slip systems: <111>{112} and <111>{110}. The energy and the stress are plotted as functions of the shear strain for the two systems in Figure 2.8. We note that the ideal strength in the easy direction is very similar for both slip systems, 7.2 GPa for <111>{112} and 7.8 GPa for <111>{110}. The energy curves for the two systems also have the same maxima. These results are common in bcc crystals [9, 22] and have their origin in the symmetry of the "saddle point" structures that govern the shear strength. Analysis of the saddle point structures for the two slip systems reveals that they are identical. Moreover, the saddle point structure in shear is precisely the bct saddle point structure that governs the orthorhombic instability in tension. The convergence of the three strain paths to the same saddle point simply shows that the nearby saddle points on the energy hypersurface act as “attractors” to which the various deformations are drawn.

While the saddle point structure for the two slip systems is the same, the strain paths on the energy hypersurface are slightly different. This difference is responsible for the fact that the strain at which the bct structure occurs is slightly larger for the <111>{110} system, and the ideal strengths for the two systems differ by ~8%. The relaxation of the crystal lattice during strain is also distinctly different. A constant volume shear on the <111>{112} system (with no relaxation in the slip plane) produces a body centered orthorhombic structure at a engineering shear strain of 33%. Allowing relaxation, the special bct structure is reached after a strain of 29% with a 4% expansion perpendicular to the slip plane, and relaxation strains in the slip plane of $< 2\%$ (see Figure 2.9 and Table 2.2). On the other hand, a <111>{110} shear reaches the bct structure at 34% strain, but requires a significant relaxation in the slip plane, the largest component being a 15% shear. The reason

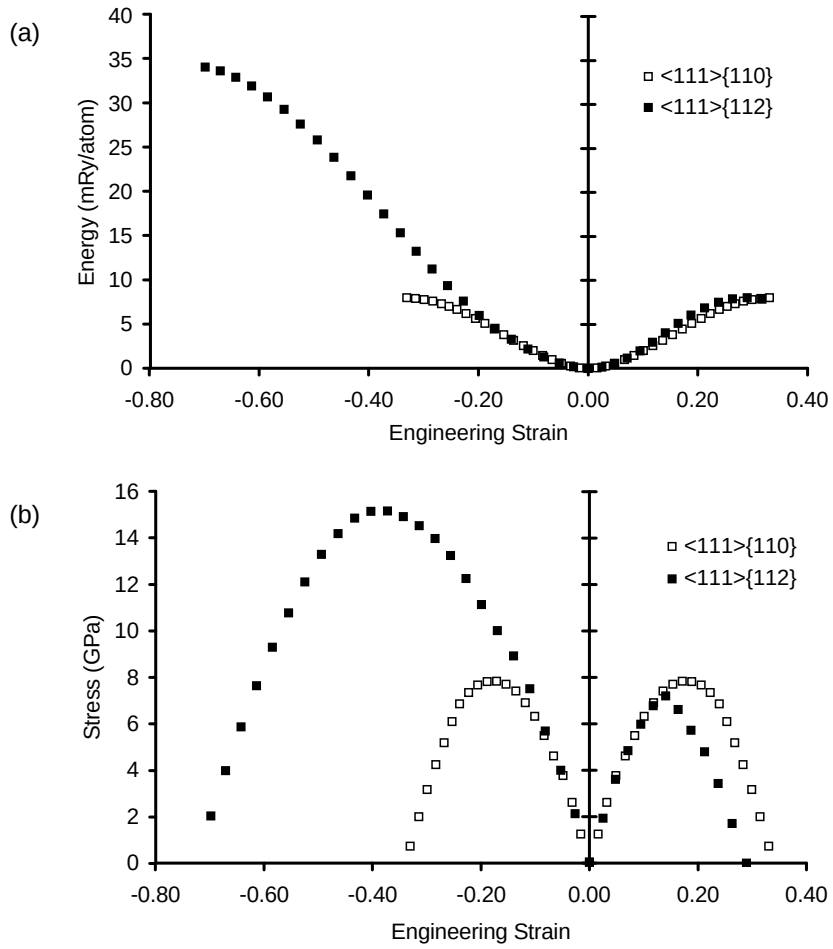

Figure 2.8: (a) Energy versus shear strain and (b) absolute value of the stress versus strain for (filled square) <111>{112} shear and (open square) <111>{110} shear.

	Tension		Shear		
	<001> Tetr.	<001> Ortho.	<111>{112} (hard)	<111>{112} (easy)	<111>{110}
σ_m, τ_m GPa	12.6	12.6	15.0	7.2	7.8
Instability	bct	ortho.	mono.	mono.	triclinic
e_{xx}	-.042	-.049	.037	-.008	-.002
e_{yy}	-.042	-.049	-.026	-.006	-.001
e_{zz}	.150	.176	.042	.028	.029
γ_{yz}			-.374	.140	.059
γ_{xz}					.020
γ_{xy}					.035
Saddle Point	fcc	bct	ortho.	bct	bct
e_{xx}	-.091	-.070	.046	.004	-.014
e_{yy}	-.091	-.070	-.031	-.016	-.015
e_{zz}	.286	.209	.088	.044	.033
γ_{yz}			-.726	.288	.339
γ_{xz}					.022
γ_{xy}		.15			.154

Table 2.2: Summary of symmetries, stresses, and strains associated with instabilities and saddle points. For tension, the strains are referred to a bct cell with the unique [001] axis along the z-axis. For <111>{112} shear, the reference structure is a base centered monoclinic cell with its 2-fold axis parallel to the x-axis, one orthogonal lattice vector parallel to the the shear direction which coincides with the y-axis, and the other orthogonal lattice vector in the y-z plane. For <111>{110} shear, the reference structure is a triclinic cell with one lattice vector in the shear direction which coincides with the y-axis, the second lattice vector in the shear plane which coincides with the x-y plane, and third vector with some component in the z-direction.

for the differences between {112} and {110} shear lies in the fact that while both paths begin at bcc and end at the bct saddle-point structure, the very different applied stresses cause them to diverge from one another at intermediate strains and produce significantly different atomic configurations near the point of instability.

As suggested by Frenkel [2], we model the ideal strength by assuming that the stress-strain relation is sinusoidal with an amplitude τ_m and period $2\gamma_B$:

$$\tau = \tau_m \sin\left(\frac{\gamma\pi}{\gamma_B}\right). \tag{2.4}$$

If we require that Hooke's law be satisfied for small strains, this implies that

$$\tau_m = \frac{\gamma_B}{\pi} G_{<111>}, \tag{2.5}$$

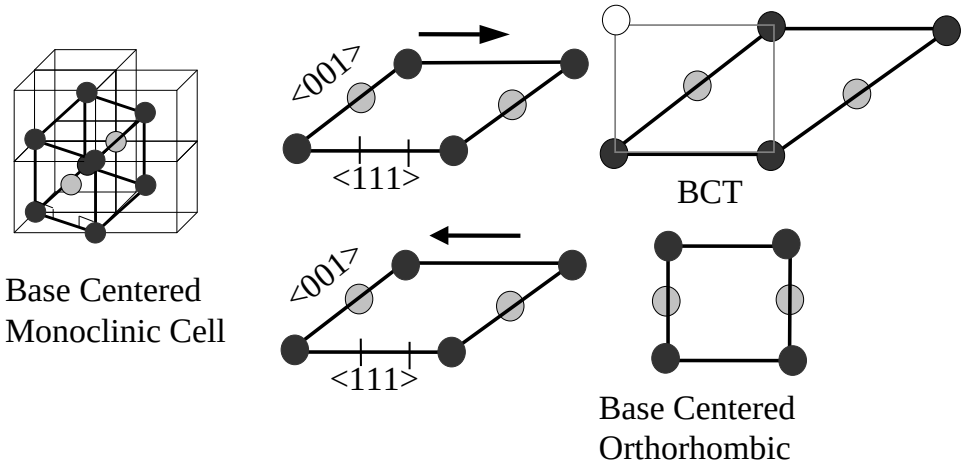

Figure 2.9: Geometry of the <111>{112} shear system. The base centered monoclinic cell is shown inside the initial bcc structure (left). A {110} projection of the structure shows the how the monoclinic cell becomes a bct cell upon applying a ∼33% shear in the easy direction (top). A shear in the opposite (hard) direction generates a base centered orthorhombic structure after a shear strain of ∼66% (bottom). The monoclinic structure's two fold axis is pointed out of the page. Black atoms are those in the closest plane and the gray atoms are in the following plane of atoms.

where $G_{<111>}$ is the shear modulus in the <111> direction. (Note that the shear moduli are the same for both shear systems.) If we take γ_B to be 0.34, then Equation 2.4 implies that $\tau_m = 0.11 G_{<111>}$. Our results give dimensionless strengths which are very close to this, for {112} $\tau/G = 0.11$ and for {110} $\tau/G = 0.12$, where we have used the experimental value of $G_{<111>}$ from Table 2.1. Using the calculated value of $G_{<111>}$the reduced strengths are 0.10 and 0.094 for shear on the {112} and {110} planes respectively.

The shear strength in the hard direction for the <111>{112} system is 15.0 GPa. It follows a path toward a different saddle point that is much higher in energy (see Figure 2.8 and 2.9). The saddle point structure is base centered orthorhombic with an a:b:c ratio of 1:1.06:1.77. This structure can also be pictured as a simple tetragonal structure with a c/a ratio of 2.42 which has undergone an (engineering) shear strain of 6% in the plane perpendicular to the unique axis. Figure 2.9 demonstrates the geometry and the fact that the strain needed to reach this saddle point is approximately twice that for shear in the easy direction.

To test the numerical accuracy of the PAW method, the energies of several structures along the <111>{112} "easy" shear path were also computed with the FLAPW technique. The energy differences were less than 0.2 mRy. While we have not confirmed that the stress states of these structures are uniaxial when computed with the FLAPW method, the close agreement in the energies along the deformation path suggests that the PAW method is quite accurate in this regime.

2.5.2 Magnetic instabilities

We also investigated the possibility that finite shear strain would induce magnetic instabilities that would limit the shear strength. This was done by testing several different magnetic structures and relaxing the stresses, as in the ferromagnetic case. The energy was only computed at a few interesting points along the <111>{112} loading path. The magnetic structures were chosen to mimic the DAFM structure used for the tensile strength calculations, but because the crystal is monoclinic along the loading path, there are several inequivalent ways of arranging the up and down spins in such a fashion. The 5 structures we studied are shown in Figure 2.10. They include superlattices made up of one or two base centered monoclinic cells, with different arrangements of the up and down spins occupying the sites.

Figure 2.11 shows the energy as a function of strain for the relaxed structures. There is a magnetic transformation at ~20% strain to the magnetic structure denoted

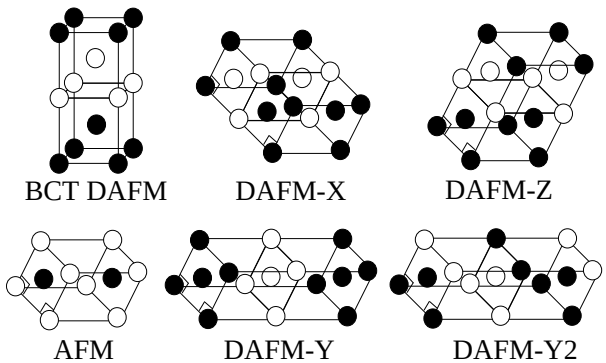

Figure 2.10: The magnetic structures used to describe complex magnetic ordering in <111>{112} shear. The structures are supercells made up of 1 or 2 body centered monoclinic cells whose 2-fold axes are oriented out of the page. The bct-DAFM structure is shown for reference.

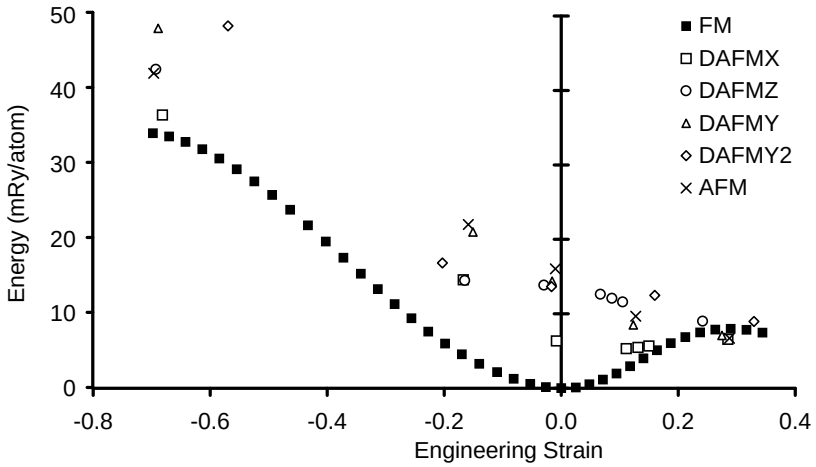

Figure 2.11: Energy as a function of shear strain for several magnetic structures. (solid square) FM, (open square) DAFMX, (open circle) DAFMZ, (open triangle) DAFMY, (open diamond) DAFMY2, (X) AFM. The various magnetic structures are shown in Figure 2.10.

DAFMX. However, this strain is beyond the point of elastic instability, so this transformation does not affect the ideal shear strength. The energy as a function of strain for the DAFMX structure was confirmed by FLAPW calculations using a method similar to that described above. We again note that we have only considered here a set of collinear structures which we hope approximate the ground state magnetic structure; however, the introduction of non-collinear magnetic ordering may further reduce the energy of some of these structures.

2.6 Ideal strength in multiaxial loading

The previous two sections have described the ideal strength of iron under several simple loading configurations: uniaxial tension and pure shear. However, in many engineering applications the stress state experienced by a material is more complex. In this section we study the strength of iron for uniaxal tension in the [001] direction in combination with biaxial tension or compression in the (001) plane. The case of unbalanced triaxial tension is commonly encountered in front of a crack tip and is thus of practical importance.

The ideal strength calculations were carried out in a manner similar to that described in Section 2.2; however, in this case the structure is relaxed to achieve the multiaxial stress state desired. For triaxial tension studied here, the stress state obeys the conditions $\sigma_{11} = 2\sigma_{22} = 2\sigma_{33}$, and for uniaxial tension plus biaxial compression the stress state can be expressed as $\sigma_{11} = -\sigma_{22} = -\sigma_{33}$. In practical terms, the desired stress state was said to be achieved when the Hellmann-Feynman stresses obey the above equalities to within 0.1 GPa.

The weak direction in tension for bcc metals is known to be the <001> direction, so we focus our attention on this orientation. Figure 2.12 shows the stress as a function of engineering strain in the <001> direction for the three different stress states considered. We see that the application of a tensile stresses perpendicular to the primary tensile direction raises the ideal tensile strength while compressive stresses decrease the ideal strength. In conjunction with this we note that the strain corresponding to the ideal strength is increased in the tensile case and decreased in the compressive case.

These results are in contrast to the often held assumption that the tensile strength of a material should decrease in a triaxial stress state. However, the reason for this result becomes clear if one examines the effect of these stresses from the perspective of their associated strains. The application of a [001] tensile strain to a bcc metal causes the symmetry to be broken and the crystal structure becomes body centered tetragonal (bct). When the

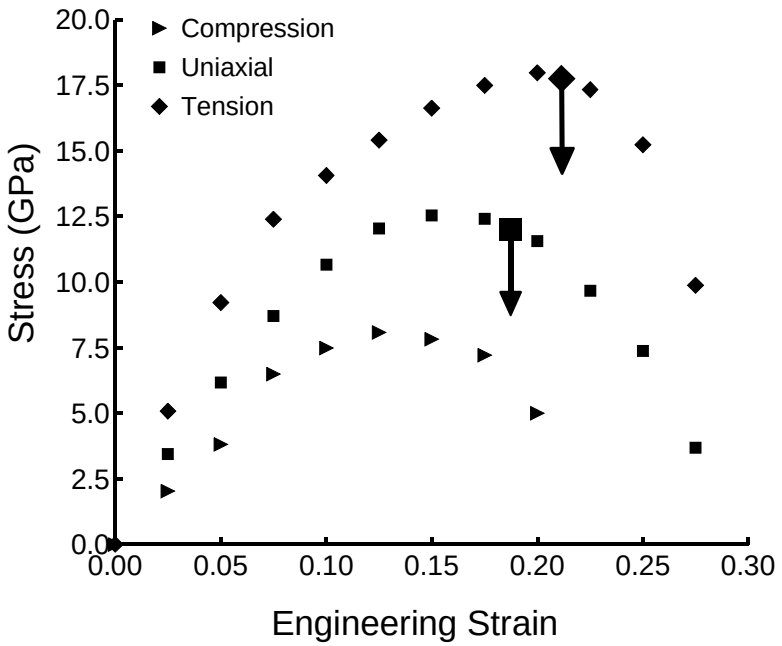

Figure 2.12: Stress as a function of strain for FM Fe under 3 different multiaxial loads: uniaxial tension plus biaxial compression (triangle), uniaxial tension (square), uniaxial tension plus biaxial tension (diamond). In all cases the largest tensile stress is in the [001] direction. The large symbols with arrows indicate the location of tetragonal to orthorhombic instabilities. The loading configuration which includes biaxial compression was not tested for this type of instability.

c/a ratio of the bct crystal is increased to $\sqrt{2}$ it becomes the fcc structure. Cubic symmetry requires that the [001] tensile stress goes to zero at both the bcc and fcc structures. As such, these structures are symmetry induced extrema (or saddle points) on the multidimensional energy-strain surface.

We can model the stress strain curve between the two energy extrema by a sinusoid as suggested by Orowon [3]:

$$\sigma = \sigma_m \sin\left(\frac{e\pi}{e_{max}}\right) \tag{2.6}$$

where σ_m is the ideal strength, e is the engineering strain, and e_{max} is the engineering strain of the second stress-free structure. Requiring that the Hooke's law be obeyed at small strain, one finds that

$$\sigma_m = \frac{e_{max}}{\pi} E_{<001>}, \tag{2.7}$$

where $E_{<001>} = 1/s_{11}$ is the Young's modulus in the <001> direction.

Now consider the effect of a constant tensile stress applied in the [100] and [010] directions. The addition of the orthogonal tensile stresses will increase the length of the crystal in the [100] and [010] directions. Because of this, a larger strain is needed in the [001] direction before one will reach the fcc structure, increasing e_{max}. Given this, Equation 2.7 implies that the ideal strength should be increased in tension. In a similar way, the addition of compressive stresses orthogonal to the tensile direction will have the opposite effect and decrease the strain needed to reach the fcc saddle point structure. In this analysis we have assumed that the stress-strain curve remains sinusoidal under multiaxial loads. In the present work, the multiaxial stresses were not a constant but rather were proportional to the applied stress. This has the effect that the fcc structure must be stress-free and thus must correspond to the equilibrium fcc structure found in uniaxial tension. However, the above analysis can still be used understand the changes in strength: the stress state at the peak of the stress-strain curve under proportional multi-axial loading would also occur during loading with constant multi-axial stresses if one makes a suitable choice for the constant multi-axial stress.

An additional effect not explicitly included in Equation 2.7 is caused by the pressure dependence of the Young's modulus. It would be possible for triaxial tensile stresses to lower the ideal tensile strength of a bcc metal if the additional stresses decreased the Young's modulus more than they increased the strain needed to reach the fcc structure. From the initial slopes in Figure 2.12, we see that triaxial tensile stresses increases the Young's modulus in iron, which increases the ideal strength even more than if the Young's modulus were

independent of pressure. This increase in the Young's modulus with pressure is consistent with the experimentally determined pressure dependence of the elastic constants [57].

As discussed in Section 2.4, the body centered tetragonal structure can become elastically unstable with respect to transformation to a face centered orthorhombic structure. For uniaxial tension in iron, this shear failure occurs at strains larger than the elastic instability associated with the tetragonal Bain path. We find that the triaxial stress state studied here increases the strain at which the tetragonal to orthorhombic transition occurs; however, the increase is less than the increase in the strain associated with the peak in the stress-strain curve (see Figure 2.12). The effect is thus to cause the orthorhombic instability to occur closer to the maxima in the stress-strain curve of the tetragonal structure for triaxial tension. In Nb, the tetragonal to orthorhombic transition occurs before the maxima in the stress-strain curve of the tetragonal structure for the uniaxial case, but becomes less favored upon applying orthogonal tensile stresses [22]. Again this moves the the orthorhombic instability closer to the peak in the stress-strain curve but from the opposite direction one finds in iron.

We have not studied the effect of pressure on the magnetic transformations that can occur along the Bain path. In the uniaxial case, the elastic instability occurs at smaller strains than these magnetic transitions and thus it dictates the ideal strength. To first order we expect that the addition of orthogonal tensile stresses would enhance the stability of the ferromagnetic phase due to a narrowing of the bandwidth, while the addition of compressive stresses would tend to favor antiferromagnetic or non-spin polarized (paramagnetic) phases. This suggests that even under multiaxial loading the ideal strength is governed by the elastic instability rather than the magnetic instability; however, a more detailed study would be needed to verify this claim as it is not known whether the change in the strain associated with the magnetic phase transitions would be larger or smaller than the change in the strain associated with the elastic instability.

2.7 Conclusions

Ab initio total energy calculations using the PAW method were used to calculate the ideal strength of iron in tension and shear. It is, to our knowledge, the first computation of the ideal shear strength for any ferromagnetic material. The ideal tensile strength in the <001> direction is 12.6 GPa and is associated with an elastic instability at 15% strain along the Bain path from bcc to fcc. At this strain the structure is stable with respect to

both orthogonal elastic instabilities and magnetic instabilities. However, if it were possible to reach larger strains, both an elastic instability toward a face centered orthorhombic structure occurs and a magnetic instability from the bct FM to a DAFM magnetic structure would be encountered.

The ideal shear strengths of the two shear systems, <111>{112} and <111>{110}, are 7.2 GPa and 7.8 GPa respectively. The ideal shear strengths are very similar because they are determined by the same body centered tetragonal "saddle point structure". (This bct "saddle-point structure" is also responsible for the orthorhombic instability in tension). Along the <111>{112} shear path, a magnetic instability toward a complex magnetic structure is found at ~20% strain. Like the magnetic instabilities in tension, it does not compromise the ideal strength because it occurs at larger strains than the elastic instability in the ferromagnetic phase.

The ideal tensile strength in the <001> direction is increased when one applies a biaxial tensile stress in the (001) plane while the strength is decreased when the additional stress is biaxial compression. This effect can be understood based on a simple crystallographic model. The triaxial stress state increases the strain needed to reach the fcc saddle point structure which results in a higher strength. The tetragonal to orthorhombic instability is found to move closer to the peak in the stress strain curve, a result similar to what is found in Nb despite the fact that they undergo different failure modes under uniaxial tension.

Despite its complex magnetic behavior and its metastable fcc phase, the ideal strength of Fe is governed by the same elastic instabilities that are found in other bcc metals.

Chapter 3

Aluminum: elastic and phonon instabilities

3.1 Introduction

Iron based alloys play an tremendous role in the field of structural materials due to their high strength to cost ratio; however, they do not appear as desirable when one is interested in a high strength to weight ratio. This is probably why very few airplanes are made of steel. Instead, the material of choice in many weight sensitive products from aircraft to high-performance bicycles is aluminum.

Aluminum is also a scientific oddity in the periodic table. While the crystal structure of most metals is identical to the other elements in their column, Al has the simple fcc structure in contrast to all the other elements in its column which have lower symmetry. (Interestingly, iron is another noticeable anomaly with regard to this trend due to the stabilizing influence of magnetism on the bcc structure).

Aluminum, along with copper, was the first material in which fully relaxed ideal shear strength calculations were performed [8]. However, recent results by Yip and co-workers suggest that there were significant errors in these first calculations [58, 59]. The present calculations were done in part to clarify this discrepancy. Also, the discovery of strain induced phonon instabilities in Al offered an opportunity to explore in detail for the first time the role of vibrational instabilities in determining the ideal strength.

Almost all previous studies of the ideal strength have focused on the strength as determined by the limit of elastic instability: at a stress equal to the ideal strength the material is internally unstable with respect to homogeneous deformation [17]. However, it is

also possible for the material to become unstable with respect to vibrational modes before it becomes elastically unstable.[1] This has been shown to be important for understanding the anomalous hardness of TiC in relation to TiN [60, 14]. In this case, the strength of TiN is limited by an optical phonon instability lowering its strength compared to that of TiC, which does not exhibit this type of instability. Other prior work in this area includes that of Li and Yip who used an empirical bond order potential to locate phonon instabilities in SiC under pure shear [61]. The present work provides the first example of a simple metal in which the ideal strength is limited by phonon instabilities. It is also the first systematic *ab initio* study of the changes in the phonon dispersion along the relaxed loading path obtained from ideal strength calculations[2].

3.2 Computational methods

In our calculations, total energies and Hellmann-Feynman stresses were determined using density functional theory while phonon frequencies were computed with density functional perturbation theory [63, 64] all within the local density approximation (LDA) [36, 35, 65]. The plane-wave pseudopotential method as implemented within the ABINIT code [66] was used. Calculations on Al used the Goedecker-Teter-Hutter Al pseudopotential [65] which required a plane wave cutoff of 32 Ry. To allow for comparisons, in a few cases supplementary calculations on Cu were performed. These computations used the Troullier-Martins pseudopotential supplied with the ABINIT code which treats the 3d electrons as valence states and required a plane wave cutoff of 80 Ry. The "Cold smearing" method of N. Marzari [67] was used for Brillouin zone (BZ) integrations with a smearing parameter of 0.04 Ry. The total energy and stress calculations used a 16x16x16 Monkhorst-Pack (MP)[41] k-point grid. The error in the stresses due to the basis set size, smearing parameter, and k-point grid was found to be $\sim$0.1GPa based on extensive convergence studies.

The ideal strength and relaxed loading path in the various directions was determined using a method described in detail previously in Section 2.2 and in Refs. [8, 9]. The lattice vectors were incrementally deformed in the direction of the applied stress. At each step the structure was relaxed such that all of the components of the Hellmann-Feynman stress tensor orthogonal to the applied stress were less than 0.1 GPa.

[1] In some respects an elastic instability can be thought of as a phonon instability with a vanishing wavevector; however, as mentioned at the end of Chapter 1, this is not entirely correct. In any case we will reserve the term phonon instability for situations in which the unstable wavevectors are away from the zone center.

[2] Some of the reseach presented in this chapter has been previously submitted for publication [62].

Our phonon studies employed the following method. First, for several structures along each relaxed loading path, an initial search for unstable modes was performed by computing the dynamical matrix on a 6x6x6 MP grid of points in the irreducible BZ using a 12x12x12 MP grid of k-points. From this information, the interatomic force constants were extracted and used to interpolate the phonon frequencies onto a finer grid of points [68, 69]. We then searched for unstable modes and noted their locations in the Brillouin zone. The phonon frequencies as a function of strain were then directly re-calculated (without interpolation) along the high symmetry directions in the BZ which exhibited unstable modes using a 20x20x20 MP grid of k-points in order to obtain high accuracy frequencies (converged to ~0.1 THz). We note that these higher accuracy frequencies were within 1 THz of those calculated earlier, indicating that the initial search parameters were reasonable.

The conditions of vibrational stability used in this work have been discussed in detail and derived by Wallace [18]. Stability requires that the phonon energies be positive for all wavevectors in the Brillouin zone. A phonon which lowers the energy of the crystal will grow in amplitude until the structure reaches a new stable state. The atomic displacements of the unstable phonon modes, and hence its crystallographic nature, can be determined from the eigenvectors of the dynamical matrix.

3.3 The quasi-static ideal strength of Al

The quasi-static ideal strength of Al was computed for <110>, <100>, and <111> uniaxial tension as well as relaxed <112>{111} shear. Before this was done, the quality of the pseudopotential was checked by performing several benchmark calculations, the results of which are presented in Table 3.1. The lattice parameter was found to be 1% too small while the elastic constants were 2-12% too big compared to experiment, typical of LDA calculations which tend to over-bind. The phonon dispersion of the equilibrium fcc structure computed using the 0K LDA lattice parameter is in excellent agreement with the experimental data obtained at 80K as shown in Figure 3.1.

3.3.1 <110> tension and <112>{111} shear

The stress-strain curves for <110> tension and <112>{111} shear are shown in Figure 3.2. For <110> tension the ideal strength is 4.9 GPa while the ideal strength for <112>{111} shear is 3.3 GPa. This result for the quasi-static ideal shear strength (3.3 GPa) is in good agreement with the recent work of Yip and co-workers [58] who obtained 2.84 GPa

	Calculated	Experimental (4K)	% Error
a_o(Å)	3.98	4.023	-1.1
c_{11} (GPa)	117.5	114.3	2.8
c_{12} (GPa)	63.5	61.92	2.6
c_{44} (GPa)	35.5	31.60	12.3
B (GPa)	81.5	79.38	2.7

Table 3.1: Lattice parameter and elastic constants of fcc Al from theory and experiment. Experimental lattice parameter was extrapolated to 4K using low temperature thermal expansion data [70]. Experimental elastic constants at 4K are from [71].

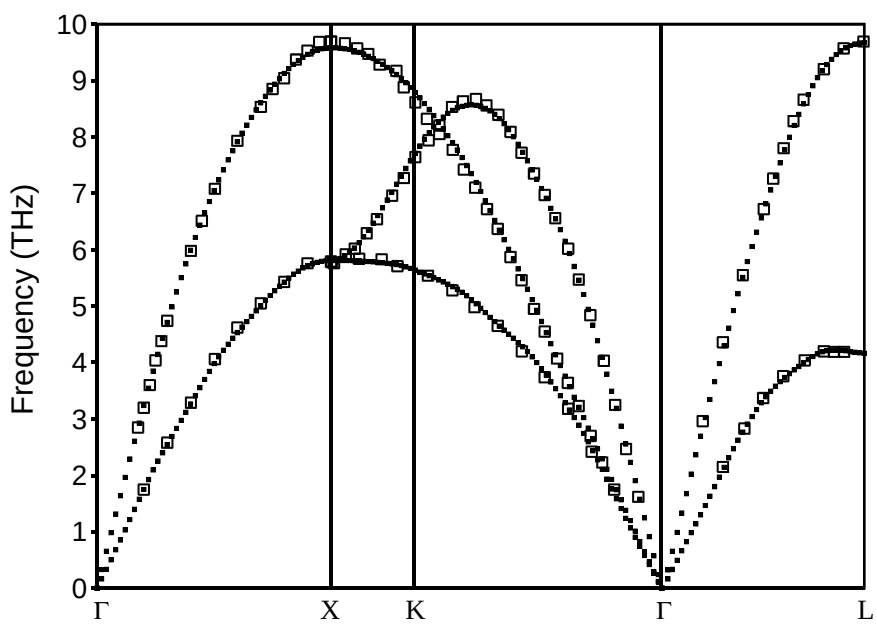

Figure 3.1: Phonon dispersion of Al measured experimentally at 80K (open symbols) [72] and calculated using the 0K LDA lattice parameter (filled symbols).

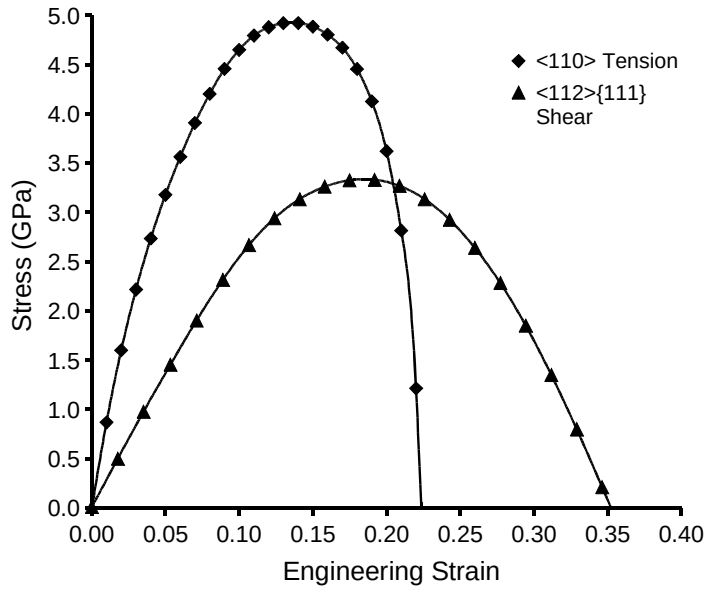

Figure 3.2: Stress versus strain for (diamonds) <110> uniaxial tension and (triangles) relaxed <112>{111} shear.

using the GGA and reported that the LDA produced strengths 10-20% higher. As noted in [58], this value is significantly larger than the first calculation of the ideal shear strength of Al [8, 59]. From Figure 3.2 we see that shear loading produces an almost perfectly sinusoidal stress-strain curve; however, the curve for <110> tension is noticeably asymmetric.

The rather steep drop-off in stress in tension near 22% strain is associated with an abrupt change in the crystal lattice as can be seen in Figure 3.3. As explained in detail below, under [110] tension the first saddle point structure that fcc metals reach is a body centered tetragonal structure in which the nearest neighbor distances in the [110] and [001] direction are equal. However, the elastic properties of Al in the fcc phase appear to result in relaxations which are not consistent with the formation of this special stress-free bct phase. Only after fairly large strains (>15%) does the structure appear to be attracted to this nearby saddle point. At this point, large adjustments in the strain relaxation pattern must be made to accommodate this preferred phase. Thus the incompatibility of the initial deformation path with the nearby saddle point causes causes an instability to occur which leads to a steep asymmetric drop-off in the stress. An examination of Cu reveals such there is no such asymmetry in the stress-strain curve for <110> tension. In this case, the elastic constants of fcc Cu produce an initial loading path that is compatible with the nearby bct saddle point (see Figure 3.3).

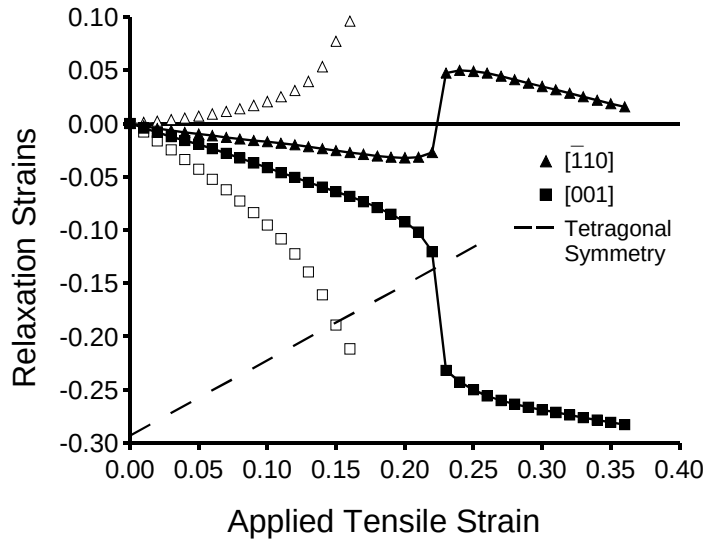

Figure 3.3: Relaxation strains in Al (filled symbols) and Cu (open symbols) due to applied tensile strain in the [110] direction: (triangles) [$\bar{1}$10] relaxation, (squares) [001] relaxation. The dashed line indicates the points where the nearest neighbor distances in the [110] and [001] directions are equal giving rise to tetragonal symmetry.

We now turn our attention to the saddle point structures for these loading configurations which can be used to understood the associated failure modes. We will first consider the symmetry of the structures along the <112>{111} loading path. The initial deformation lowers the symmetry of the fcc crystal to base centered monoclinic. At an engineering shear strain of 35%, a stress-free body centered tetragonal (bct) structure with a c/a ratio of 0.8 is reached (see Figure 3.2 and 3.4). If one continues to strain in this direction, the structure is once again base centered monoclinic until a strain of 71% is reached, at which point it attains the fcc structure. However, the stacking sequence of the (111) planes has shifted from ABCABCABC in the initial fcc structure to ACBACBACB in the final fcc structure as seen in Figure 3.4.

We can now examine the changes in symmetry during tensile loading in the <110> direction. A small tensile strain in the <110> direction causes the symmetry of the fcc crystal to be broken at which point it becomes body centered orthorhombic (bco) as shown in Figure 3.4. It continues with this symmetry until the nearest neighbor distances in the <110> and <001> become equal at which point the structure reaches the higher symmetry bct saddle point structure. This structure is stress free and corresponds to the stress-strain curve in Figure 3.2 crossing the x-axis at 22% strain. This bct saddle point structure has a c/a ratio of 0.8 and is identical to the saddle point structure that occurs during <112>{111}

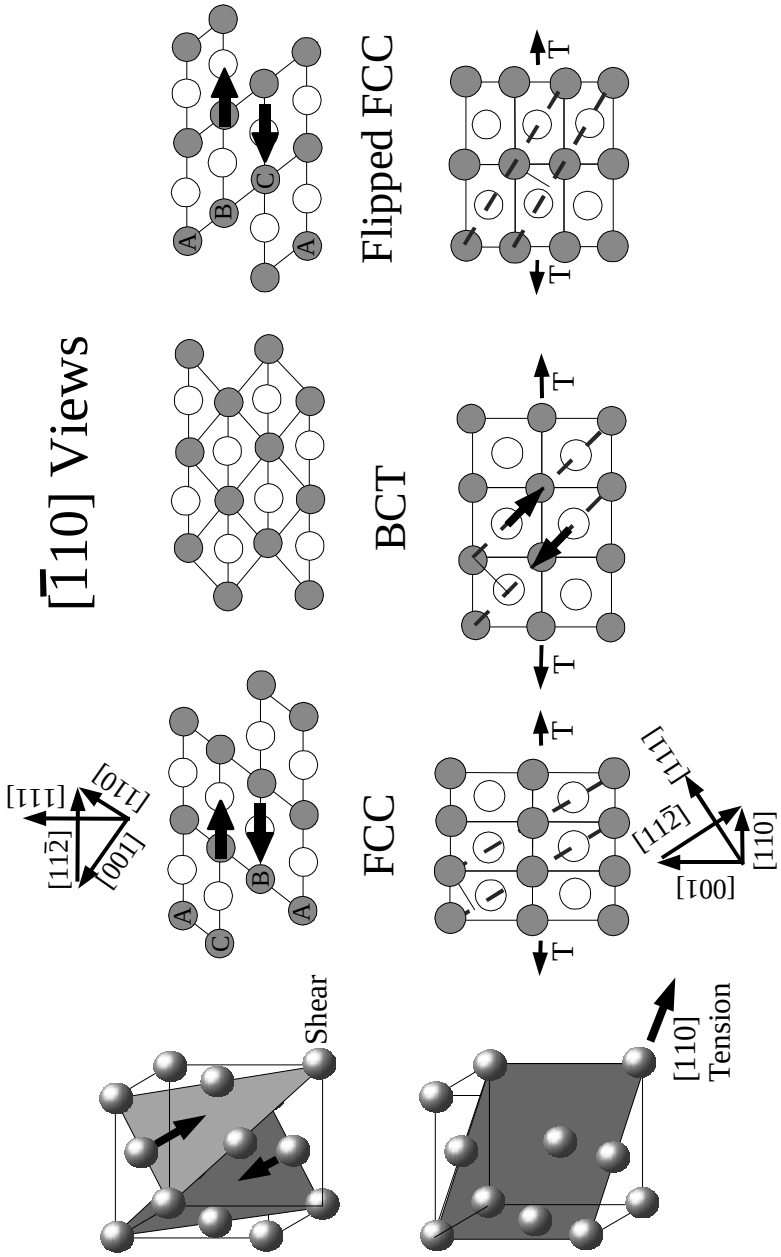

Figure 3.4: Schematics showing the evolution of the crystal structure during $[11\overline{2}](111)$ shear (top) and [110] tension (bottom). The two dimensional figures are views in the $[\overline{1}10]$ direction. The gray atoms are in the closest (110) plane while the while atoms are in the (110) plane behind it. These gray/white atom positions are repeated in successive (110) planes. For both loading configurations the structure changes from fcc to a stress-free bct structure to a rotated fcc structure.

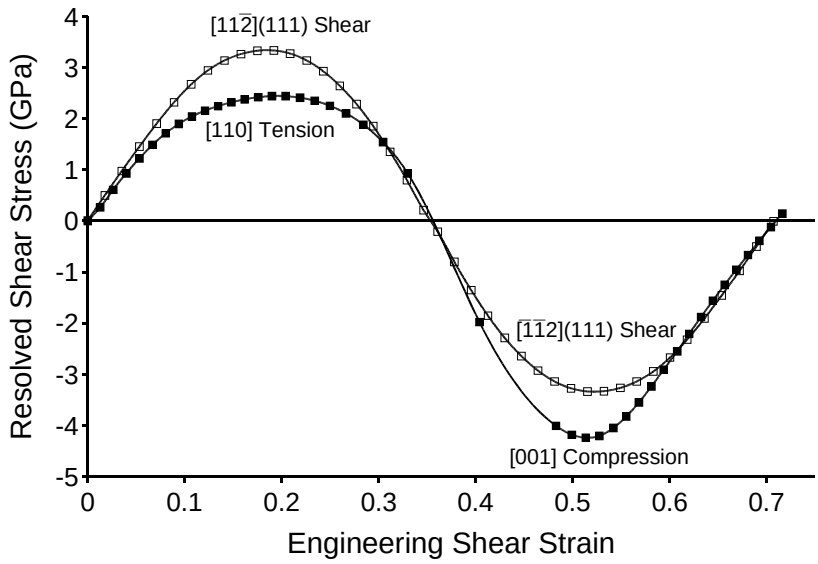

Figure 3.5: Resolved shear stress as a function of engineering shear strain for Al along the loading paths corresponding to [110] uniaxial tension (filled symbols) and relaxed [11$\bar{2}$](111) shear (open symbols). Following the curves backward from 71% shear strain corresponds to [001] uniaxial compression (filled symbols) and relaxed [$\bar{1}\bar{1}$2](111) shear (open symbols).

shear. If one continues to load the crystal in the <110> direction, the structure again becomes bco with the nearest neighbor distance in the <001> direction less than that in the <110> direction. Finally, at a strain of 41%, another high symmetry structure is reached. The crystal has once again become fcc except that it is now rotated by 90° around a [$\bar{1}$10] axis relative to the starting structure (Figure 3.4). The fact that the fcc crystal structure is regenerated by this loading configuration suggests that while the loading corresponds to uniaxial tension, the deformation produced is shear in character. In fact, the changes in geometry are very similar to those found in <112>{111} shear. Not only do both loading paths have the same saddle point configuration, but they both produce the same rotated fcc structure upon further deformation. (The 90° rotation found during <110> tension actually results in the same configurational changes as shifting the stacking sequence from ABCABCABC to ACBACBACB as seen in Figure 3.4).

Based on this analysis we conclude that the failure mechanisms associated with <110> tension and <112>{111} shear are in fact identical, irrespective of the fact that one is the result of tensile loading while the other is the result of shear loading. However, surprisingly the maximum resolved shear stress at which failure occurs in both cases is significantly different as shown in Figure 3.5. The ideal tensile strength in the <110> direction is 4.9 GPa which results in an resolved shear stress of 2.4 GPa while the ideal

strength for <112>{111} shear is 3.3 GPa. Thus the resolved shear strength in pure shear is 27% larger than that in tension despite the fact that both loading configurations result in the same failure mechanism. This result is not unique to this loading configuration or this material.

For example, if one starts at the fcc structure at the end of the loading paths described above and moves backward toward the bct saddle point, the strength for <112>{111} shear is identical to that found in the forward direction (3.3 GPa) as it should be due to the symmetry of the loads. However, if one moves backward from the final fcc structure along what was originally the <110> tensile loading path (but can now be described as a <001> compression of the final structure) the maximum resolved shear stress is 4.2 GPa which is much higher than it was in the forward direction (2.4 GPa) or in pure shear (3.3 GPa), see Figure 3.5. We note that <001> compression leads to the same bct saddle point as $[\overline{1}\overline{1}2](111)$ shear leading us to conclude that they have the failure mode which is also identical to that found in <110> tension.

A second example can be found by examining Cu. In this case the ideal tensile strength in the <110> direction is 6.0 GPa which gives rise to a resolved shear stress of 2.9 GPa; however, the ideal strength for relaxed <112>{111} shear is 2.6 GPa. In this case the strength in pure shear is *smaller* by 12%.

Thus in Al we have found that the resolved shear stress at which failure occurs is 2.4 GPa, 3.3 GPa, and 4.23 GPa in <110> tension, <112>{111} shear, and <001> compression respectively even though the failure mechanisms are identical. In Cu, the results are opposite with strengths of 2.9 GPa and 2.6 GPa in <110> tension and <112>{111} shear respectively (see Table 3.2). This also has the interesting result that Al is stronger than Cu under pure shear loading while Cu is stronger than Al when the shear failure is caused by tensile loading in the <110> direction. The source for these difference can be understood by examining the relaxation strains in each case.

We can define a orthogonal coordinate system where the applied shear is in the x direction and acting on the plane normal to the z direction with the y direction chosen to form a right handed coordinate system. For $[11\overline{2}](111)$ shear in fcc materials, this corresponds to x=$[11\overline{2}]$, y=$[\overline{1}10]$, and z=[111]. The relaxation strains in each of these three directions are plotted as a function of applied engineering shear strain in Figure 3.6 for <112>{111} shear in Al.

Although the structure at any point along the <110> loading path has at least orthorhombic symmetry, we can treat it as a special case of a monoclinic structure in which

		Ideal strength (GPa)	Maximum resolved Shear Stress (GPa)
Al	<112>{111} shear	3.3	3.3
	<110> tension	4.9	2.4
	<001> compression	8.5	4.2
Cu	<112>{111} shear	2.6	2.6
	<110> tension	6.0	2.9

Table 3.2: Ideal strengths of Al and Cu for <110> tension, <001> compression, and <112>(111) shear as well as the maximum resolved shear stress acting on the <112>(111) shear system for each loading configuration.

the lattice vectors are chosen to mimic the structure during <112>{111} shear. Based on this new geometry it is possible to compute the relaxation strains as a function of engineering shear strain using the same coordinate system as was used for the case of <112>{111} shear. The results of this calculation are shown in Figure 3.6. The structures are equally spaced with respect to the tensile strain in the <110> direction; however, once the structures have been converted to their monoclinic equivalents they are no longer equally spaced along the applied shear strain axis.

Examining Figure 3.6, we see that in relaxed <112>{111} shear the largest relaxation corresponds to an expansion perpendicular to the shear plane ($e_{[111]}$ increases in the positive direction). A similar behavior is seen in <110> tension but the curve is shifted significantly to lower applied shear strains. If we resolve the applied <110> tensile stress into shear and normal components on the {111} plane we see that in addition to the shearing stress on the <112>{111} system there is a normal stress acting to expand the crystal in the <111> direction, see Figure 3.7. This stress causes the expansion to occur faster in tensile loading than in the pure shear case. Since the crystal would like to expand in the <111> direction during the shear, the normal stress that occurs in <110> tension helps facilitate this shear and hence lowers the resolved shear strength.

This argument can also be formulated in terms of thermodynamics. Under both loading paths the crystal starts in the equilibrium fcc state and transforms to the stress-free bct saddle point structure. Since both the initial and final states are identical in the two loading configurations, it is clear that the total energy added to the system in both cases must also be identical. In the relaxed shear loading case, there is only one non-zero stress and thus, the change in energy is simply the area under the corresponding stress-strain curve in Figure 3.5. Now in <110> tension we have non-zero stresses in several directions. In this

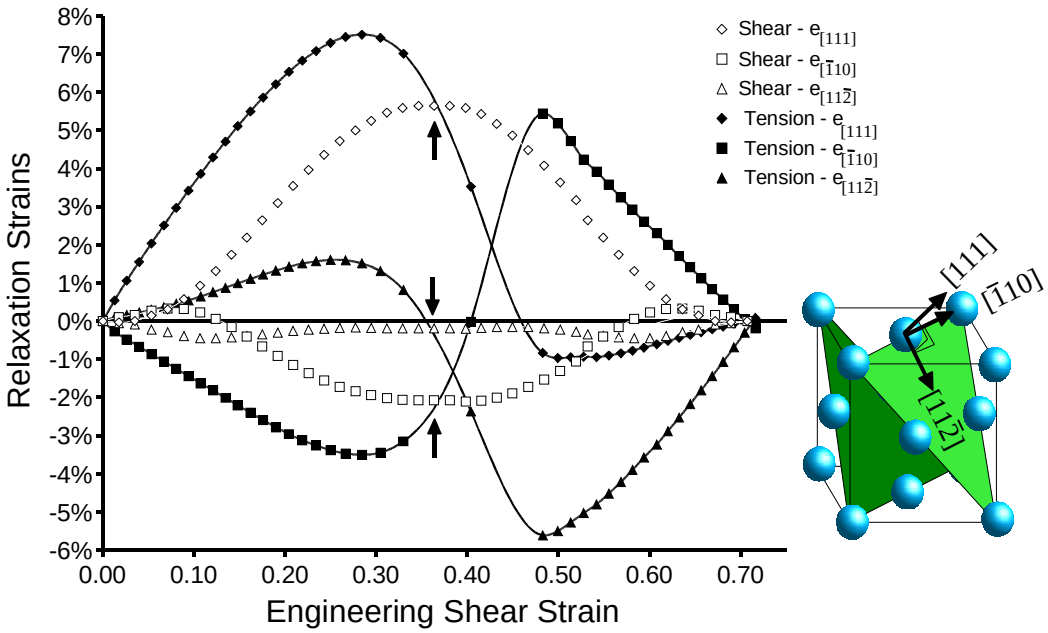

Figure 3.6: Relaxation strains as a function of engineering shear strain for Al along the loading paths corresponding to <110> uniaxial tension (filled symbols) and relaxed <112>{111}shear (open symbols). On the left side, which corresponds to [110] tension and $[11\overline{2}](111)$ shear, the largest relaxations are in the same direction for both tension and shear. However, on the right side, which corresponds to [001] compression and $[\overline{11}2](111)$ shear, the relaxations are in different directions. Along the tensile loading path, the relaxations undergo a dramatic changes near 35% strain. At this strain, the corresponding relaxation strains for the tensile and shear paths are equal to each other (as emphasized by the arrows), demonstrating that both paths cross through the same saddle point structure.

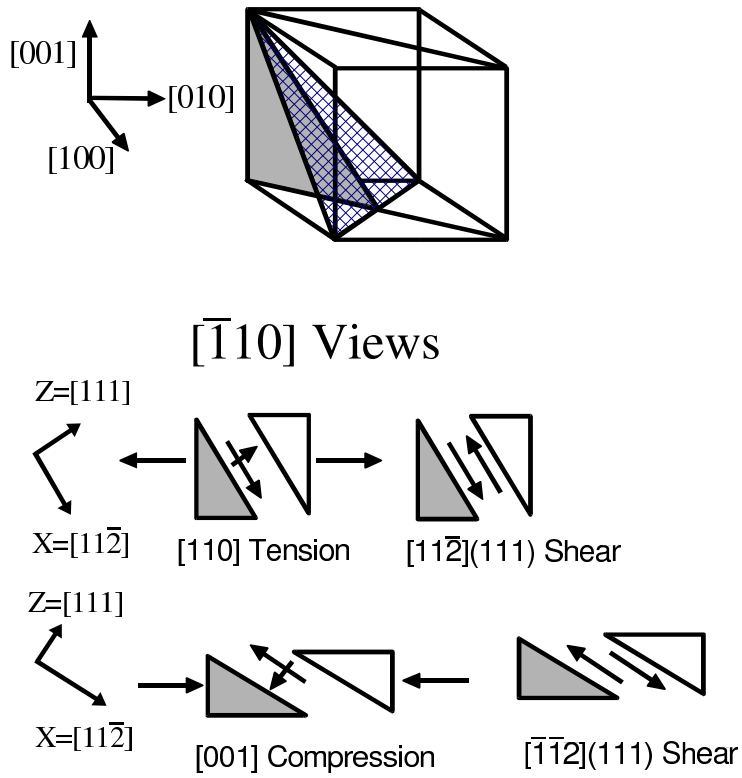

Figure 3.7: Schematics illustrating the direction of the normal and shearing stresses resolved on the (111) plane for different loading configurations. The gray shaded plane in the 3-dimensional picture corresponds to the gray shaded planes in the [$\bar{1}$10] views. We see that [110] tension is similar to [11$\bar{2}$](111) shear but also includes a normal stress acting to expand the crystal in the [111] direction. In addition, [001] compression is similar to [$\overline{11}$2](111) shear but also includes a normal stress acting to compress the crystal in the [111] direction.

case the stresses are acting in the same directions as the corresponding strains needed to move the crystal from the fcc structure to the bct structure.[3] Therefore, the elastic energy is increased by all the components of the stress. Since the sum of these contributions must equal the total change in energy in the relaxed shear case, the contribution from the applied shear stress must be smaller in the tensile case than in the pure shear case. Based on this, the area under the stress-strain curve in Figure 3.5 must be smaller for the tensile case than for the pure shear case. Since the shear strains at the beginning and end of the curve are fixed by the saddle points, one expects the peak stress will be smaller in the tensile case assuming the stress-strain curves do not have pathological shapes. Returning to Figure 3.5 we see that the peak stress is in fact smaller in the tensile case as this argument suggests.

A similar argument can be applied to understand the other changes in the resolved shear strength mentioned previously. Starting at the fcc structure located at the end of the loading path, a $[\overline{11}2](111)$ shear backward toward the starting configuration requires a maximum resolved shear stress of 3.3 GPa, the same as is found in the forward direction. The relaxation strains along this path are identical to the forward path as well due to symmetry. As described above one can also follow the path obtained during [110] tension backward from the final fcc structure by compressing the final structure in the [001] direction. In this case the compressive stress can be resolved on the (111) plane resulting in a shear stress in the $[\overline{11}2]$ direction and a compressive normal stress acting in the $[\overline{111}]$ direction (see Figure 3.7). The compressive stress causes the crystal to contract in the [111] direction as seen in Figure 3.6. This is clearly in opposition to the desired expansion in this direction. However, because the strains needed to reach the saddle point are fixed by the structure, the crystal must expand at some point in order to reach the saddle point. When this occurs the stress in the $[\overline{111}]$ direction will be in the opposite direction as its corresponding strain and thus the system will loose energy in this process. If the net effect of the stresses conjugate to the relaxation strains is to lower the system energy, the area under the stress-strain curve corresponding to the resolved shear stress must be larger in the tensile case than in the relaxed shear case. As a result, the maximum resolved shear stress in this loading configuration is higher than that found in pure shear, consistent with what we observe in Figure 3.5.

This analysis is also consistent with the behavior of other metals. Unlike Al, during relaxed <112>{111} shear Cu does not expand in the <111> direction – a result

[3] In tension, $e_{[\bar{1}10]}$ is acting in the opposite direction one finds in the relaxed shear case; however, the magnitude of this strain is small compared to the others for both the tensile and relaxed shear loading configurations.

previously reported and explained in terms of the experimentally determined third order elastic constants [8, 73]. However, during <110> tension Cu expands in the <111> direction due to the resolved normal stress in this direction. Since the crystal prefers to shear with no perpendicular expansion, the effects of the resolved normal stress in <110> tension act to make the shearing process more difficult, increasing the resolved shear strength.

A similar argument can also be applied to the case of multiaxial loading in Fe as described in Section 2.6. In that case relaxed [001] tension requires a contraction in the [100] and [010] directions. Tensile stresses in the [100] and [010] act to oppose this relaxation and as a result the tensile strength is increased. Compressive stresses act in the direction of the relaxation and thus lower the tensile strength. Because the multiaxial loading condition studied in Section 2.6 is proportional (i.e. $2\sigma_{[001]} = \sigma_{[100]} = \sigma_{[010]}$), the uniaxial stress state and the multiaxial stress states will have the same stress-free fcc saddle point. Therefore, the above strain energy analysis can be applied in precisely the same way as it was in Al. We also note that if one used a different multiaxial loading condition in which a constant biaxial stress is applied orthogonal to the applied stress, the above argument would not apply as the fcc saddle point would have a different volume from the one found in uniaxial tension and, thus, it would have a different energy and tensile strain.

These examples suggest that changes in the resolved shear strength can be understood by examining whether the orthogonal stresses act to assist or hinder the relaxations that the crystal prefers.

3.3.2 <100> tension and <111> tension

We now turn our attention to the the ideal strength under two other loading configurations: <100> and <111> uniaxial tension. The ideal strength in these directions is 12.9 GPa and 11.3 GPa respectively which is considerably larger than <110> tension. The stress strain curves are shown in Figure 3.8. In both cases, no stress-free saddle point structures are found, but rather the peaks in the stress-strain curves are associated with saddle points at infinite strain. This is clear from the shape of the stress-strain curves in addition to the fact that the stresses have not reached zero even after strains of 100%. Because these instabilities are associated with a saddle point at infinity, they would result in cleavage fracture. These results are in good agreement with the previous work of Li and Wang who reported strengths of 12.7 and 11.5 GPa in the <100> and <111> directions respectively [74].

While the peak in the stress-strain curve corresponds to the ideal strength in most cases, a material can become internally unstable before this point is reached [17]. In par-

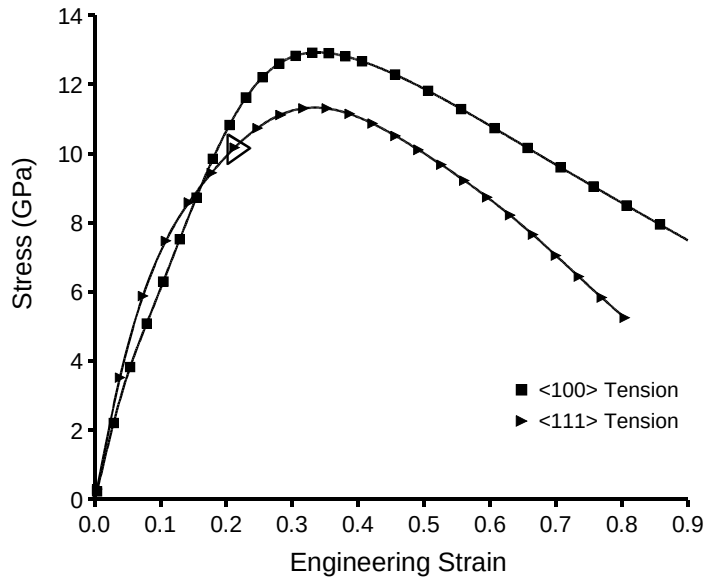

Figure 3.8: Stress versus engineering strain for uniaxial tension in the (squares) <100> direction and (triangles) <111> direction. The large open triangle indicates the location of the orthogonal elastic instability that occurs during <111> tension.

ticular, any instability whose eigenvector is orthogonal to the loading direction will not be visible in the stress-strain response. Such is the case for Al loaded in <111> tension: an elastic instability orthogonal to the loading direction occurs near 25% strain. In order to examine the conditions of stability in detail, we have computed the eigenvalues of the symmetrized Wallace tensor along the loading path (see Figure 3.9). Recall that internal stability requires that the symmetrized Wallace tensor be positive definite [17], and thus a material becomes unstable when at least one eigenvalue of the symmetrized Wallace tensor becomes negative. While tedious, the computation of the Wallace tensor as a function of strain is straight forward. At a given point along the relaxed loading path, one applies six small (∼1%) orthogonal strains and computes the stress tensor associated with each. By suitable choice of the strains, it is trivial to solve for the 36 components of the Wallace tensor.[4]

The elastic instability in <111> tension is clearly seen in Figure 3.9 at 25% strain. The minimum eigenvalue in this case is doubly degenerate and has an eigenvector corresponding to shear in the [111] direction (i.e. parallel to the 3-fold symmetry axis) and on any plane which contains this direction. Thus, in <111> tension Al undergoes a shear fail-

[4]Unlike the the calculation of elastic constants of a stress-free crystal, care must be taken to use deformations which do not produce rotations due to the fact that the the material is under a finite load.

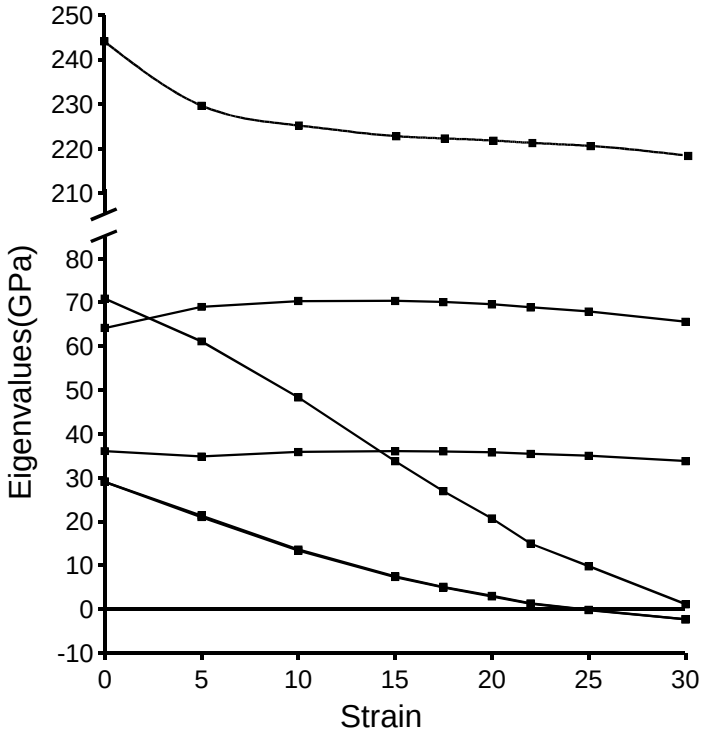

Figure 3.9: Eigenvalues of the symmetrized Wallace tensor as a function of strain for uniaxial tension in the <111> direction. The lowest eigenvalue is doubly degenerate due to symmetry, and at 25% strain it becomes negative indicating the material is elastically unstable. At 31% strain the second smallest eigenvalue goes to zero corresponding to the tensile modulus in the <111> direction vanishing at the peak in the stress-strain curve.

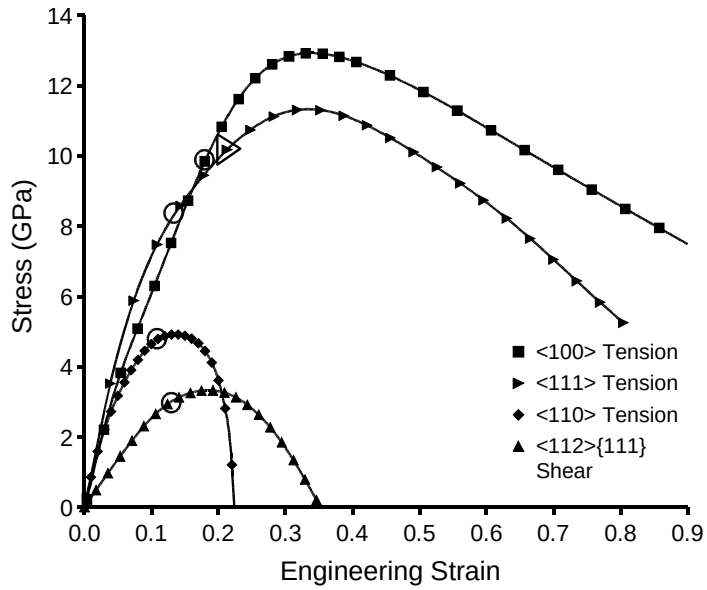

Figure 3.10: Stress-strain curves for <110>, <100>, and <111> uniaxial tension as well as relaxed <112>{111} shear. Open circles indicate the location of phonon instabilities. The large triangle indicates the location of the orthogonal elastic instability that occurs in <111> tension. The lines are guides for the eye.

ure at 25% strain before one reaches the peak in the stress strain curve at 33% strain. Due to this orthogonal instability, the ideal strength in <111> tension is reduced from 11.3 GPa to 10.7 GPa.

3.4 Phonon instabilities in aluminum and its ideal strength

As described in Section 3.2, a search was performed to locate possible phonon instabilities in Al under <100>, <111>, and <110> uniaxial tension, as well as relaxed <112>{111} shear. Phonon instabilities were found to occur along all four loading paths. The locations of these instabilities are shown as open circles superimposed on the relaxed stress-strain curves in Figure 3.10. In each case the phonon instability occurs before the peak of the stress strain curve; however, in <110> tension and <112>{111} shear the phonon instabilities are located at strains much closer to the elastic instability than is the case in <100> and <111> tension. This indicates that the phonon instabilities in <100> and <111> tension should significantly reduce the ideal strength in these directions, while in <110> tension and <112>{111} shear the value of the ideal strength is not strongly affected by the phonon instabilities as summarized in Table 3.3.

Loading configuration	Phonon instability		Elastic instability		Shear system of phonon instability
	σ(GPa)	e	σ(GPa)	e	
[110]tension	4.89	0.115	4.92	0.140	$[\overline{1}\overline{1}2](111)$
$[11\overline{2}](111)$ shear	3.16	0.145	3.33	0.185	$[\overline{1}\overline{1}2](111)$
[001]tension	9.20	0.170	12.92	0.340	[001](100)
					$[1\overline{1}10](11\overline{1})$
[111]tension	8.95	0.150	10.7	0.25	[111](001)
					[111](110)
					$[111](\overline{1}10)$
					$[111](\overline{1}\overline{1}1)$

Table 3.3: Stresses and strains associated with phonon instabilities as compared to the elastic instabilities in the same direction. Also shown are the shear plane and displacement associated with the phonon instabilities.

The phonon dispersion as a function of strain are shown in Figure 3.12-3.15. We only show here high symmetry directions in the Brillouin zone along which phonon instabilities were found to occur. Also, only the branch corresponding to the polarization which goes unstable is shown to simplify the figures. For convenience we use the negative y-axis to plot imaginary frequencies. In general we see the softening of various phonon branches occurring gradually as the strain is increased. At the largest strains, the initial slope of the dispersion curves become negative indicating that the material is unstable with respect to homogeneous deformation (long wavelength distortions) and is thus elastically unstable.

In Figure 3.11(a) we see that in [110] tension a phonon instability develops around 11% strain. At this strain, the instability has a [111]/3 wavevector, but larger wavevectors quickly become unstable as the strain is increased slightly. Analysis of the eigenvectors of the dynamical matrix indicates that the unstable mode corresponds to displacements in approximately the $[\overline{1}\overline{1}2]$ direction. Thus the failure is a $[\overline{1}\overline{1}2](111)$ shear failure in which the displacements have a periodicity of 3 (111) planes. Interestingly, this periodicity is commiserate with the ABCABC stacking of the (111) planes found in the fcc structure.

We now consider the instability that occurs during $[11\overline{2}](111)$ shear. In this case, the instability first occurs at a wavevector between [111]/3 and [111]/2 at an engineering shear strain of 14% (Figure 3.11(b)). The unstable mode has displacements in the $[\overline{1}\overline{1}2]$ direction resulting in a $[\overline{1}\overline{1}2](111)$ shear failure with a periodicity of 2 or 3 (111) planes. To confirm this result, we performed calculations on supercells consisting of 2 unit cells stacked in the (111) direction. We used the previously relaxed structures along the loading path to set the cell geometry but shifted the internal coordinates of the second atom resulting in a

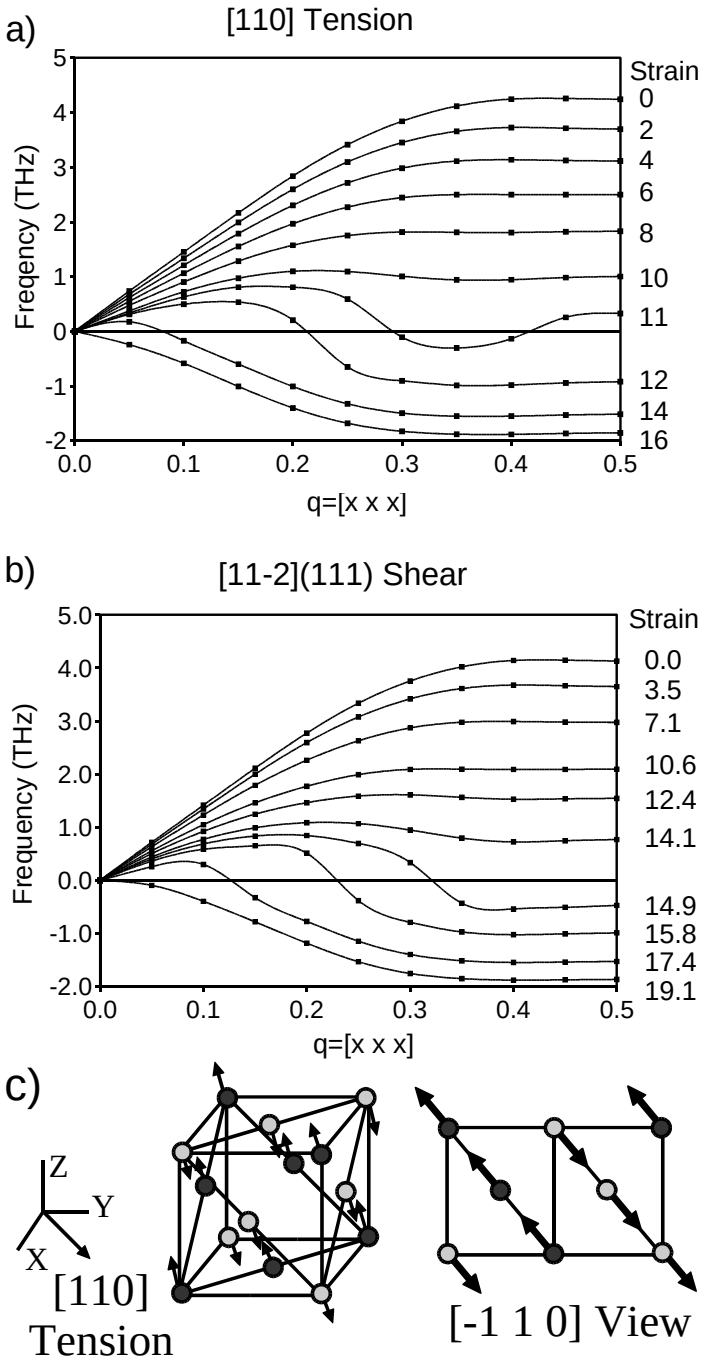

Figure 3.11: Phonon frequencies as a function of strain for (a) [110] tension and (b) $[11\overline{2}](111)$ shear. The curves are labeled according to the applied strain as indicated on the right side of the figure. Lines are spline fits which are guides to the eye. (c) Schematic illustrating the crystallography of the instability at the zone edge.

$[\overline{1}\overline{1}2]$ shift in alternate (111) planes. The internal forces were computed for the structures along the loading path and it was found that initially the internal forces were acting against the shift of the planes. However, the forces decreased with strain until a strain of 14% at which point the forces reached zero and then continued to grow in magnitude in the opposite direction. At strains larger than 14% the internal forces were working to increase the magnitude of the shift indicating that the introduced "frozen" phonon would grow in amplitude.

The geometry of the instability that occurs in <110> tension is identical to that found in <112>{111} shear (Figure 3.11(c)). This is probably because <110> tension can be visualized as a superposition of <112>{111} shear and an expansion perpendicular to the shear plane. The two deformation modes also exhibit elastic instabilities which are very similar as described in Section 3.3.1.

A different type of instability is found in [001] tension. Instabilities are found to occur with wavevectors in two separate regions of the Brillouin zone. At around 17% strain an instability occurs at $[11\overline{1}]/2$ followed by another at around 18% near 2[100]/3. We find that the displacements in the two cases correspond to periodic $[1\overline{1}0](11\overline{1})$ shear and [001](100) shear respectively. A schematic of the crystallography of these instabilities is shown in Figure 3.12(b). Increased strain causes the region of unstable wavevectors to grow significantly until the material becomes elastically unstable at strains which correspond to the peak of the stress strain curve.

Of the four loading configurations studied, the electronic origin of this instability is the most clear. Figure 3.13(a) shows the electronic density of states as function of strain along the relaxed loading path. The feature near -0.1 Ha at zero strain moves to higher energies with increasing strain and reaches the Fermi level at 20% strain where the phonon instability occurs. This movement of this feature corresponds to the bottom of the second band at the X-point ([100] direction) increasing to the extent that it reaches the Fermi level at 20% and thus becomes de-populated (see Figure 3.13(b)). This can also be seen by examining the Fermi surface as a function of strain shown in Figure 3.14. As the crystal is strained in the [001] direction the extent of the intrusion of the Fermi surface into the second zone in the [100] and [010] directions decreases. At the strain which corresponds to the phonon instability this pocket of electrons completely vanishes destabilizing the structure. A similar though less dramatic event occurs during [110] tension at the strain corresponding to the phonon instability. The fact that the phonon instabilities in Al are related to its electronic structure is also consistent with the fact that preliminary calculations found no

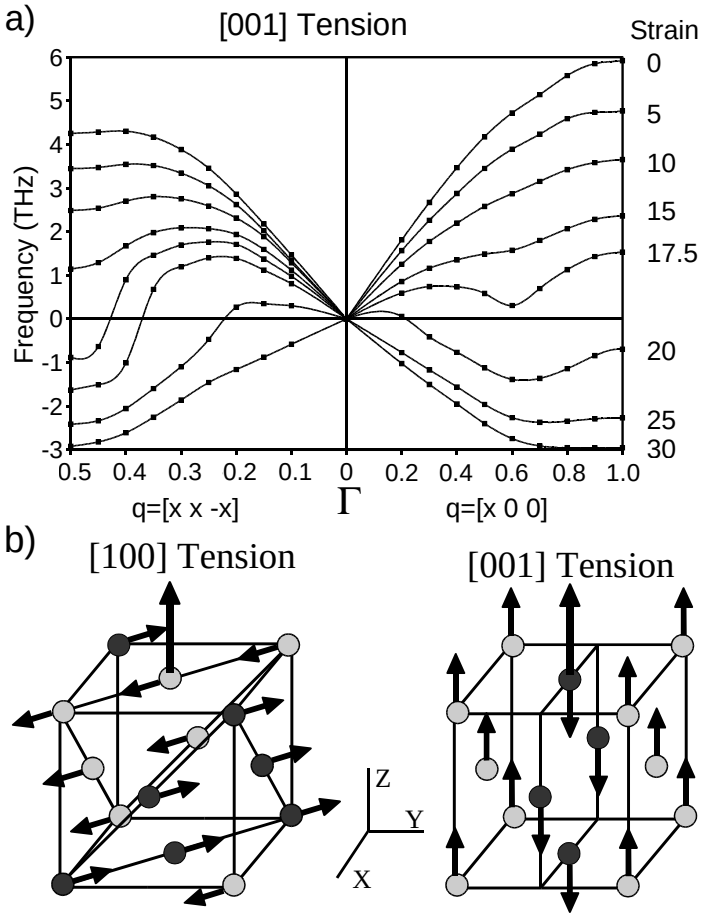

Figure 3.12: (a) Phonon frequencies as a function of strain for [001] tension. (b) Schematic of the instabilities.

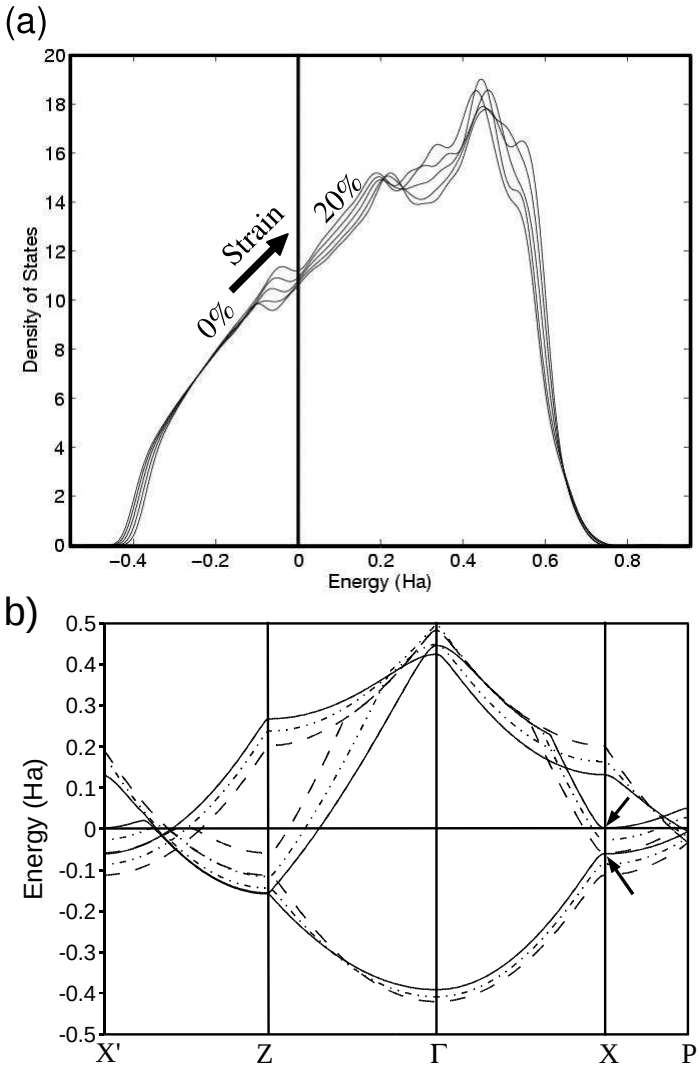

Figure 3.13: (a) Electronic density of states as a function of strain in the [001] direction for 0%, 5%, 10%, 15%, and 20% strain. The energies are plotted relative to the Fermi energy which is taken as 0. (b) Band structure for 0% (dashed line), 10% (dot-dashed line), 20% (solid line) strains. Coordinates of symmetry points in units of $2\pi/a$: X=(1 0 0); Z=(0 0 a/c); P=(1 0 a/2c); X'=(1 0 a/c) (Also see Figure 3.14). Arrows emphasize the gap at the X point for 20% strain.

such phonon instabilities in Cu which has the same crystal structure but a very different Fermi surface.

Finally, the case of [111] tension is the most complex. Phonon instabilities develop along four different high symmetry directions. In all cases, the phonon first become unstable between 15% and 17.5% strain as seen in Figure 3.15. Analysis of the eigenvectors of the dynamical matrix leads to the result that all the phonon instabilities are shear in character with the atomic displacements in the [111] direction but with different shear planes (see Table 3.3). We also note that around 20% strain the long wavelength wave velocity becomes imaginary in the $[\bar{1}10]$ direction. The eigenvectors of this instability coincide with the elastic stability described in Section 3.9. In that section, calculations of the Wallace tensor as a function of strain indicated that the instability occurs at ~25% strain which is slightly larger than the result from the phonon method. However, there is some uncertainty in the value computed with the phonon method due to the fact that it is difficult to determine the phonon frequencies close to the gamma point because a large number of k-points are required. As such, it is possible that at 20% strain the slope near the gamma point is in fact positive initially and then becomes negative and this can simply not be resolved due to the finite interval between the points at which the frequencies were computed.

For the four cases studied here we have shown that even in tensile loading, the failure mode of Al is shear in nature. Al is known to be ductile even a low temperatures and does not exhibit cleavage fracture. This is consistent with our results which further suggest that shear failure is an inherent property of Al even in an initially dislocation-free perfect crystal.

3.5 Conclusions

The quasi-static and vibrational ideal strengths of aluminum have been calculated for <110>, <100>, and <111> uniaxial tension, as well as relaxed <112>{111} shear. The quasi-static failure modes in <110> tension and <112>{111} shear are identical despite the different loading configurations. This can be seen by examining the saddle point structures along the loading paths. Although the failure modes are the same in these two cases, the maximum resolved shear stresses along the loading paths are quite different. It is found that these differences can be understood by examining the relaxation patterns of the strains orthogonal to the primary deformation. The resolved shear strength is decreased when the relaxation strains are in the same direction as those found under relaxed shear. This idea

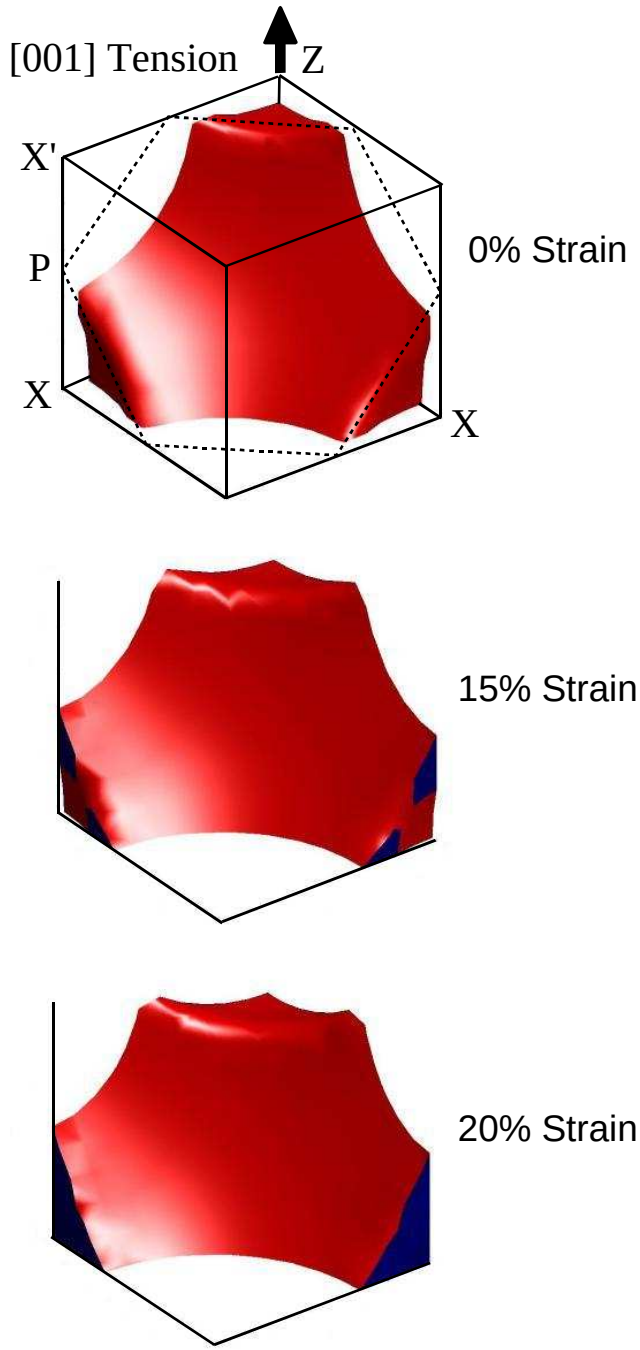

Figure 3.14: One-eighth of the Fermi surface of Al as a function of strain in the [001] direction. The surface shown corresponds to the second zone and thus the states behind this surface are not occupied by electrons. The Brillouin zone edges are superimposed on the surface corresponding to 0% strain.

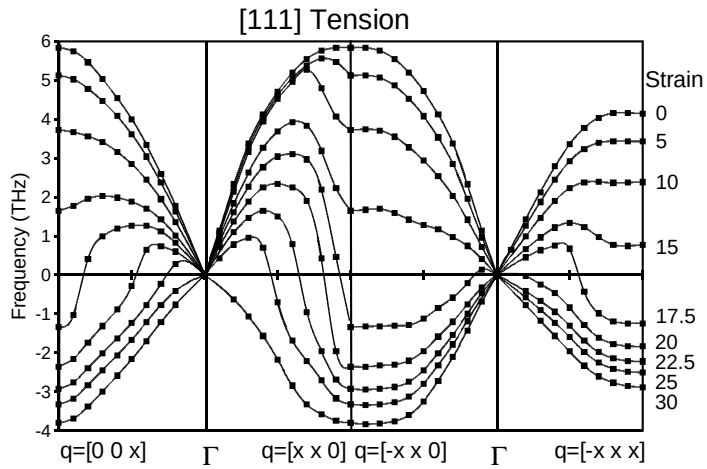

Figure 3.15: Phonon frequencies as a function of strain for [111] tension.

can also be used to understand the increase in the resolved shear strength of Al under <001> compression as well as the changes in the shear strength of Cu with loading configuration. A thermodynamic argument is presented to explain this result.

The quasi-static stress-strain curves for Al in <100> and <111> uniaxial tension are presented. In both cases, there are no stress-free saddle points along the relaxed loading path. Instead the peak in the stress-strain curves correspond to a saddle point at infinite strain. In <111> tension, an orthogonal elastic instability is found at 25% strain lowering the strength in this direction. This instability is associated with a doubly degenerate eigenvalue of the symmetrized Wallace tensor vanishing and corresponds physically to shear in the <111> direction on any plane which contains this direction.

The limits on the strength of Al imposed by vibrational instabilities has been explored by computing the phonon dispersion as a function of strain using density functional perturbation theory for <110>, <100>, and <111> uniaxial tension, as well as relaxed <112>{111} shear. In all four cases, phonon instabilities occur at points away from the center of the Brillouin zone before the material becomes unstable with respect to homogeneous deformation. This is the first time the ideal strength of a metal has been shown to be dictated by phonon instabilities. We go on to describe the crystallography of the unstable modes, all of which are shear in character. These results further suggests that shear failure is an inherent property of aluminum even in an initially dislocation-free perfect crystal.

Chapter 4

Summary and future work

4.1 Summary

While it is difficult to calculate many mechanical properties directly from first principles due to their sensitivity to microstructure, there are some properties which can be calculated quantitatively with good accuracy using *ab initio* methods. The research presented in this dissertation has focused on one such property – the ideal strength.

The stress required to cause a material to become mechanically unstable determines the ideal strength. Most previous studies have focused on the limits implied by stress induced elastic instabilities. However, large strains can produce other effects which may destabilize the lattice before any elastic instability occurs. This dissertation has included detailed studies of two such phenomena: magnetic phase transformations and phonon instabilities.

In Chapter 2, the effects of magnetic instabilities on the ideal strength of Fe have been considered in detail. That work included the first ideal shear strength calculation of a ferromagnetic material. The ideal strength of Fe in both tension and shear is determined by the same elastic instabilities found in other bcc metals which is a somewhat surprising result given the fact that the bcc structure in Fe is an anomaly caused by its magnetism. However, magnetism does play an important role as it allows Fe to simultaneously have the high dimensionless strength associated with other bcc metals while at the same time having the nearby low-energy fcc phase which is integral to the thermal processing of its microstructure.

In Al, it is found that the resolved ideal shear strength is highly sensitive to the loading configuration even when the configurations lead to the same saddle point structure and produce the same failure mode. The strength is decreased in situations in which the

multi-axial stresses orthogonal to the applied shear act to produce strains consistent with the strains found under relaxed shear. This effect can be understood by analyzing the elastic energy associated with the various stress components.

Chapter 3 also included the first detailed *ab initio* study of the changes in the phonon dispersion along the ideal strength loading path. For all of the loading configurations studied in Al, phonon instabilities are found to intrude before the material becomes elastic unstable. This is the first known example of a simple metal in which the ideal strength is limited by phonon instabilities. These instabilities appear to be a unique feature caused by the electronic structure of Al and not simply the result of it crystal structure as no such instabilities are found in Cu. This is somewhat unusual, as the ideal strength has been found in most cases to be dictated by the symmetry of the crystal. The phonon instabilities in Al are all shear in nature which suggests that even a dislocation-free perfect crystal at 0K will exhibit shear failure.

4.2 Future Work

4.2.1 Temperature dependence of the ideal strength

All of the calculations presented in this thesis correspond to materials at 0k. Since most engineering applications occur at higher temperatures, a method for determining the temperature dependence of the ideal strength would be extremely helpful. A first estimate of the changes in the ideal strength with temperature can be found by scaling the strength by the change in the elastic modulus in that direction with temperature. Experimental data on the temperature dependence of the elastic constants for many materials, including most common metals is available, making this approach attractive [57]. This approximation is in the spirit of the Orowon or Frenkel models for the ideal strength in which the ideal strength scales linearly with the modulus in that direction. For this to hold true, one must assume that the strain associated with the peak in the stress-strain curve remains constant; however, this fact remains to be verified. Calculations are underway to study the temperature dependence of the ideal strength from first principles and determine to what extent it can be accounted for by the changes in the elastic constants with temperature [75].

The ideal tensile strength of Ta is being computed as a function of temperature within the quasi-harmonic approximation. Ta was chosen because it is a bcc metal and thus the computation of the tensile strength only requires the relaxation of a single parameter. The computation proceeds as follows. A two dimension grid of structures is created in which

the applied strain is incremented along one axis and the relaxation strain is incremented along the other axis. For each structure the phonon spectra is then computed on a MP grid of points in the irreducible Brillouin zone. From the phonon dispersion data, the free energy as function of temperature (at constant strain) can be computed using statistical mechanics. One then repeats the phonon and free energy calculations for all the structures of interest. From this data, one can now select a single temperature and compile the results of the free energy at this temperature for the entire set of structure creating a free energy surface as a function of the two strain variables. A polynomial or spline fit to this surface can be differentiated in the two directions and the maximum stress along the relaxed loading path can be obtained yielding the ideal strength at that temperature.

There are a few difficulties with this approach. When one reaches the peak in the stress-strain curve, the material is elastically unstable. This creates problems for computing the free energy in this regime. Thus one can only compute the energy up to strains just below the ideal strength (or any phonon instabilities). One then hopes that smooth fits through the data will allow for an accurate extrapolation to slightly higher strains. The other main difficulty is the computational resources needed to compute the phonon dispersion on ~50-100 different structures (approximately 100 computer weeks). However, by computing a few structures at a time over a period of many months these calculations are expected to be completed by the time this thesis is submitted. Finally, we note that the use of the quasi-harmonic approach limits the temperature range for which these calculations are valid to approximately 1/2 of the melting temperature. This is due to the fact that anharmonic contributions become more important at higher temperatures. There is also decreased accuracy at high temperatures due to the fact that the contribution to the free energy from thermally produced vacancies (and other defects) is not accounted for.

Based on these calculations it should be possible to determine the temperature dependence of many thermodynamic properties in addition to the ideal strength without requiring significant additional computer time. These properties include temperature dependence of the thermal expansion coefficient, the bulk modulus, the heat capacity, as well as the elastic constants c_{11} and c_{12}. Figure 4.1 presents preliminary results on the temperature dependence of the thermal expansion coefficient. A first glance suggest that the agreement with experiment is fairly good, though a more analysis is currently underway. Comparison of the computed thermodynamic data with experiment will also provide information on the range of validity of the quasi-harmonic approximation which has previously been studied in detail for only a few metals.

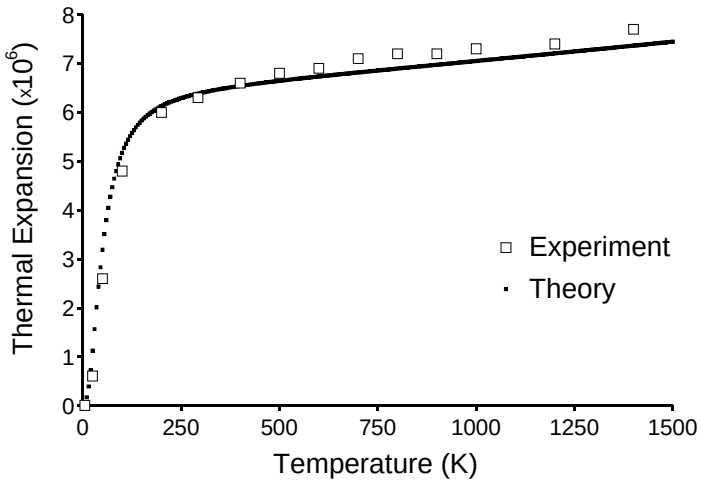

Figure 4.1: Linear thermal expansion coefficient of Ta as a function of temperature from experiment (open symbols) [70] and computed within the quasi-harmonic approximation (filled symbols).

4.2.2 Analysis of nanoindentation data

The best experimental measure of the ideal strength at the present time comes from the nanoindentation of thin films with low defect densities. During these experiments a small diamond indenter is pressed into the surface of a single crystal. The initial response is elastic up until some critical load at which point the material suddenly deforms plastically creating an excursion in the load-displacement curve.

Unfortunately, a direct comparison of theory and experiment is difficult due to the complex stress state developed under the indenter. As we have seen in Section 3.3.1, the ideal strength and the stress-strain curve depend on the details of the loading configuration even when the failure mode does not change. At the same time, the stress-strain curve determines the stress state developed under the indenter, further complicating the analysis. Krenn et al. [12] have used finite element modeling (FEM) in combination with density functional calculations to analyze the nanoindentation of W and Mo. A number of simplifying assumptions were made in this analysis. The FEM problem was treated in a radially symmetric fashion rather than treating the full three dimensional problem which may more accurately represent the effects of anisotropy. Also, the dependence of the ideal strength of the stress state was only considered in an approximate way.

For materials in which the ideal strength is highly sensitive to the multiaxial stress state (such as Al) an alternate approach may be more appropriate. A linear elastic FEM solution of the full anisotropic 3-dimensional problem using the elastic constants can be

performed to determine an approximate range for each strain component under the indenter. One can then create a regularly spaced grid in 6-dimensional space which covers these ranges. The strains specified by the points on the grid can then be used to create structures for density functional calculations. These calculations are used to compute the stresses which correspond to these strains. An interpolation or curve-fitting scheme can then be used to create a anisotropic constitutive relation which is valid for all the strains of interest. This is then used as input into the 3-dimensional FEM simulation. A final check of the strains produced in this simulation can be performed to ensure that the strains under the indenter fall within the range used to create the constitutive relation. From this calculation one now knows the stress distribution at points along the load-displacement curve, which can then be compared to experiment. Specifically one can determine the stresses associated with the point on the experimental load-displacement curve at which the material first undergoes plastic deformation.

Bibliography

[1] A. Kelly and N.H. MacMillian, Strong Solids, (Clarendon Press, Oxford 1986), 3rd ed. pp. 1-56.

[2] J. Frenkel, Z. Physik 7, 323 (1926).

[3] E. Orowon. Rept. Prog. Phys. 12, 185 (1949).

[4] A.T. Paxton, P. Gumbsch, and M. Methfessel, Phil. Mag. Lett. 63, 267 (1991).

[5] M. Šob, L. G. Wang, and V. Vitek. Comp. Mat. Sci. 8, 100 (1997).

[6] M. Šob, L. G. Wang, and V. Vitek V. Kovove Materialy 36, 145 (1998).

[7] J.W. Morris Jr., C. R. Krenn, D. Roundy, and Marvin L. Cohen, in Phase Transformations and Evolution in Materials, edited by P. E. Turchi and A. Gonis (The Minerals, Metals and Materials Soc., Warendale, PA, 2000), pp.187-207.

[8] D. Roundy, C. R. Krenn, Marvin L. Cohen, and J. W. Morris Jr., Phys. Rev. Lett. 82, 2713 (1999).

[9] D. Roundy, C. R. Krenn, Marvin L. Cohen, and J. W. Morris Jr., Phil. Mag. A 81, 1725 (2001).

[10] J. W. Morris Jr., C. R. Krenn, D. Roundy, and M. L. Cohen, Mat. Sci. Eng. A 309, 121 (2001).

[11] J. W. Morris Jr., Z. Guo, C. R. Krenn, and Y. H. Kim, ISIJ International 41, 599 (2001).

[12] C. R. Krenn, D. Roundy, Marvin L. Cohen, D. C. Chrzan, and J. W. Morris, Jr., Phys. Rev. B 56, 134111 (2002).

[13] J. W. Gibbs, Trans. Conn. Acad. 3, 108-248 (1876) (Scientific Papers of J. Willard Gibbs, Vol. 1: Thermodynamics, Ox Bow Press, 1993, p 184-215).

[14] Seung-Hoon Jhi, S. G. Louie, Marvin L. Cohen, and J. W. Morris, Jr. Phys. Rev. Lett. 87, 075503/1-4 (2001).

[15] R. Hill, Math. Proc. Camb. Phil. Soc. 77, 225 (1975).

[16] R. Hill and F. Milstein, Phys. Rev. B, 15, 3087 (1977).

[17] J. W. Morris Jr. and C. R. Krenn, Phil. Mag. A 80, 2827 (2000).

[18] D. C. Wallace, Thermodynamics of Crystals, (J. Wiley, New York 1972).

[19] D. M. Clatterbuck, D. C. Chrzan, and J. W. Morris Jr., Phil. Mag. Lett. 82, 141 (2002)

[20] D. M. Clatterbuck, D. C. Chrzan, and J.W. Morris, Jr. Acta Materialia, 51,2271 (2003).

[21] M. Šob, L. G. Wang, and V. Vitek, Mat. Sci. Eng. A 234-236, 1075 (1997).

[22] Weidong Luo, D. Roundy, M. L. Cohen, and J. W. Morris Jr., Phys. Rev. B 66, 094110 (2002)

[23] F. Milstein and J. Marschall, Phil. Mag. A 58, 365 (1988).

[24] R. W. K. Honeycombe and H. K. D. H. Bhadeshia, Steels: Microstructure and Properties, second edition (Edward Arnold, London, 1995).

[25] R. M. McMeeking and D. M. Parks in Elastic-Plastic Fracture, ASTM STP 668, edited by J. D. Landes, J. A. Begley, and G. A. Clarke (American Society for Testing and Materials, Philadelphia, 1979), pp. 175-194.

[26] H. C. Herper, E. Hoffman, and P. Entel, Phys. Rev. B 60, 3839 (1999).

[27] D. J. Singh, W. E. Pickett, and H. Krakauer, Phys. Rev. B 43, 11628 (1991).

[28] D. J. Singh, Planewaves, Pseudopotentials and the LAPW method (Kluwer Academic, Boston, 1994).

[29] P. E. Blöchl, Phys. Rev. B 50, 17853 (1994).

[30] P. Hohenberg and W. Kohn, Phys. Rev. 136, B864 (1964).

[31] W. Kohn and L. J. Sham, Phys. Rev. 140, A1133 (1965).

[32] G. Kresse and J. Hafner, J. Phys. Condens. Matter 6, 8245 (1994).

[33] G. Kresse G and J. Furthmüller, Phys Rev. B. 54, 11169 (1996).

[34] G. Kresse and D. Joubert, Phys. Rev. B 59, 1758 (1999).

[35] J. P. Perdew and A. Zunger, Phys. Rev. B 23, 5048 (1981).

[36] D. M. Ceperly and B. J. Alder, Phys. Rev. Lett. 45, 566 (1980).

[37] S. H. Vosko, L. Wilk, M. Nusair, Can. J. Phys. 58, 1200 (1980).

[38] J. P. Perdew, J. A. Chevary, S. H. Vosko, K. A. Jackson, M. R. Pederson, D. J. Singh, and C. Fiolhais Phys. Rev. B 46, 6671 (1992).

[39] Y. Wang and J. P. Perdew, Phys. Rev. B 44, 13298 (1991).

[40] P. E. Blöchl, O. Jepsen, and O. K. Andersen, Phys. Rev. B 49, 16223 (1994).

[41] H. J. Monkhorst and J. D. Pack, Phys. Rev. B 13, 5188 (1976).

[42] M. Methfessel and A. T. Paxton, Phys. Rev. B 40, 3616 (1989).

[43] P. Blaha, K. Schwarz, and J. Luitz, WIEN97, A Full Potential Linearized Augmented Plane Wave Package for Calculating Crystal Properties. (Vienna: Karlheinz Schwarz, Techn. Univ. Wien 1997). ISBN 3-9501031-0-4 Updated version of P. Blaha, K. Schwarz, P. Sorantin, and S. B. Trickey, Comp. Phys. Commun. 59, 399 (1990).

[44] M. Acet, H. Zahres, E. F. Wassermann EF, and W. Pepperhoff, Phys. Rev. B 49, 6012 (1994).

[45] J. A. Rayne and B. S. Chandrasekhar, Phys. Rev. 122, 1714 (1961).

[46] B. D. Cullity, Introduction to Magnetic Materials, (Addison-Wesley, Reading Mass., 1972) p617.

[47] K. Knöpfle, L. M. Sandrastskii, and J. Kübler Phys. Rev. B 62, 5564 (2000).

[48] V. P. Antropov, M. I. Katsnelson, M. van Schilfgaarde, B. N. Harmon Phys. Rev. Lett. 75, 729 (1995).

[49] O. N. Mryasov, V. A. Gubanov, and A. I. Liechtenstein Phys. Rev. B 45, 12330 (1992)

[50] M. Korling and J. Ergon Phys. Rev. B 54, 54 (1996).

[51] D. M. Bylander and L. Kleinman Phys. Rev. B 60, R9916 (1999).

[52] Y. Tsunoda, J. Phys. Condens. Matter. 1, 10427 (1989).

[53] Y. Tsunoda, Y. Nishioka, R. M. Nicklow, J. Magn. Mag. Mat. 128, 133 (1996).

[54] L. Stixrude, R. E. Cohen, and D. J. Singh, Phys. Rev. B 50, 6442 (1994).

[55] M. Friák, M. Šob, V. Vitek, Proceedings of the International Conference Juniormat 2001, Institute of Materials Engineering, Brno University of Technology, Brno 2001, p. 117.

[56] S. S. Brenner, J. Appl. Phys. 27, 1484 (1956).

[57] D. F. Nelson (ed.), Landolt-Bornstein LBIII/29a – Low Frequency Properties of Dielectric Crystals: Second and Higher Order Elastic Constants, (Springer-Verlag, Berlin, 1992).

[58] Shigenobu Ogata, Ju Li, S. Yip, Science 298, 807 (2002).

[59] Subsequent invesitgation has revealed that there were errors made in constructing the pseudopotential used in Ref. 8. Weidong Luo, D. M. Clatterbuck, J. W. Morris, and Marivin L. Cohen, Unpublished Research (2002).

[60] C. R. Krenn, J. W. Morris, Jr. S. -H. Jhi and J. Ihm, in Hard Coatings Based on Borides, Carbides, and Nitrides, edited by A. Kumar, Y. -W. Chung and R. W. J. Chia (TMS, Warrendale, PA, 1998), pp. 379-388.

[61] Ju Li and S. Yip, Computer Modeling in Engineering and Science 3, 219, (2002).

[62] D. M. Clatterbuck, C. R. Krenn, Marvin L. Cohen, and J. W. Morris, Jr., Submitted for review.

[63] S. Baroni, P. Giannozzi and A. Testa Phys. Rev. Lett. 58, 1861 (1987).

[64] X. Gonze and J.-P. Vigneron, Phys. Rev. B 39 13120, (1989).

[65] S. Goedecker, M. Teter, and J. Hutter, Phys. Rev. B 54, 1703 (1996).

[66] X. Gonze, J.-M. Beuken, R. Caracas, F. Detraux, M. Fuchs, G.-M. Rignanese, L. Sindic, M. Verstraete, G. Zerah, F. Jollet, M. Torrent, A. Roy, M. Mikami, Ph. Ghosez, J.-Y. Raty, D.C. Allan. Computational Materials Science 25, 478-492 (2002), http://www.abinit.org.

[67] N. Marzari, Ph. D. Thesis, Cambridge University, 1996.

[68] X. Gonze, Phys. Rev. B 55, 10337 (1997).

[69] X. Gonze and C. Lee Phys. Rev. B 55, 10355 (1997).

[70] Y. S. Touloukian et. al. (eds.), Thermal expansion: metallic elements and alloys, (IFI:Plenum, New York, 1975).

[71] G. N. Kamm and G. A. Alers, J. Appl. Phys. 35, 327 (1964).

[72] R. Stedman and G. Nilsson, Phys. Rev. 145, 492 (1966).

[73] C. R. Krenn, D. Roundy, J. W. Morris, Jr., and M. L. Cohen, Mat. Sci. Eng. A, A317, 44-48 (2001).

[74] W. Li and T. Wang. J. Phys. Condens. Matter. 10, 9889 (1998).

[75] D. M. Clatterbuck and C. R. Krenn. Unpublished research (2003).